

# Mesoscale Variability and Vertical Shear Instabilities

## Downstream of the Denmark Strait

Author: Julián Marcelo Morales Meabe

Supervisors: Eleanor Frajka-Williams and Joel Bracamontes Rodríguez

Date: 31st December 2014



## ABSTRACT

This study investigates the variability of the Denmark Strait Overflow Water (DSOW) and its interaction with overlying ambient water, focusing on their distinct physical characteristics and implications for regional mixing and transport. DSOW, characterized by colder, faster, and fresher properties with dominant along-stream velocity along the isobaths, contrasts with the warmer, slower, and saltier ambient waters, which propagate westward across isobaths. These layers, delineated by a constructed reference interface layer ( $L_R$ ), exhibit mesoscale variability dominated by a 1.8-day period that accounts for approximately 50% of velocity and temperature fluctuations. Cyclonic and anticyclonic eddies, detected along the reference layer, induce significant vertical isopycnal displacements, alternately elevating and depressing the isopycnals. These mesoscale features may influence the frequent vertical shear instabilities ( $Ri < \frac{1}{4}$ ) observed within the DSOW layer, particularly below the reference layer, potentially through changes in stratification and vertical shear. Such instabilities, possibly amplified by high-frequency oscillations linked to mesoscale activity, underscore the complex interplay between eddy dynamics, stratification, and shear-induced mixing, shaping the interactions between DSOW and its surrounding waters.



## 1. Introduction

The Denmark Strait is one of the few connections between the Nordic Seas and the open Atlantic Ocean along the Greenland-Scotland ridge. Its specific location makes it a region of special oceanographic interest due to its role in the sources of variability of the Atlantic Meridional Overturning Circulation (AMOC). Through this strait warm water is transported northward via the North Icelandic Irminger Current (NIIC), whereas cold water is transported southward into the Atlantic Ocean via the North Icelandic Jet (NIJ), and the East Greenland Current (EGC). At the sill of the Denmark Strait these currents converge, as shown in [figure 1](#), producing complex interactions between them and modifying their properties. It is here where Denmark Strait Overflow Water (DSOW) is formed ([Harden et al., 2016](#)), a dense water mass that spills over the sill and spreads over the bottom into the Atlantic Ocean. Eventually the DSOW is transported into the Deep Western Boundary Current (DWBC) or the Spill Jet ([Von Appen et al., 2014](#)).

Despite its depth the transport of DSOW into the Atlantic Ocean has a relevant velocity component, with maximum mean speeds surpassing 0.6 m/s at determined locations ([Voet & Quadfasel, 2010](#)). The reason for these high speeds seems to be related to the steepness of the bathymetry and its high density, since it is a gravity driven current. Downstream the Denmark Strait's sill this bottom water gains speed due to the increasing bathymetry and the tilting of pycnoclines ([Girton, 2001](#)). It is in this region where a phenomenon called entrainment develops. Entrainment is responsible for the mixing of dense overflow water with the lighter waters above it (often referred to as ambient water), resulting in changes in the transport and the physical properties of the overflow plume ([Von Appen et al., 2014](#)). Previous studies attribute these mixing processes to the roughness of the topography (inducing near the bottom turbulence); vertical shear instabilities between the fast DSOW and the waters above; and the propagation of

eddies downstream inducing stirring ([Voet & Quadfasel, 2010](#)). These processes contribute to the variability of DSOW thus influencing the formation of North Atlantic Deep Water (NADW) and therefore the variability of the AMOC.

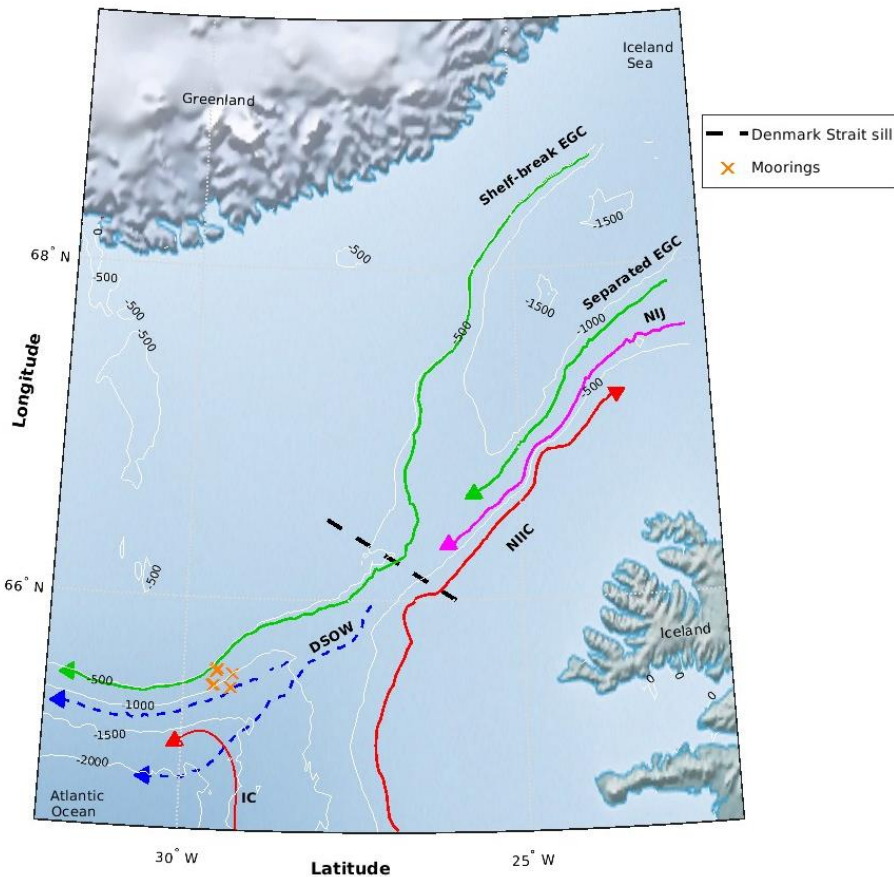


**Figure 1.** Denmark Strait schematic circulation and location of moorings. Green arrows show the paths of the two different branches of the EGC. Magenta arrow shows the path of the NIJ. Red arrows show the paths of warm waters with origins in the Irminger Sea, the IC and the NIIC. The blue dashed arrows show the paths of the deep DSOW.

Continuous monitoring of the sill and downstream of the sill has shown that the variability in the transports of the DSOW does not follow a seasonal pattern, but the maximum variability takes

place in the order of days. These findings suggest that mesoscale activity plays a key role in the variability of the DSOW ([Voet & Quadfasel, 2010](#); [Von Appen et al., 2017](#); [Moritz et al., 2019](#)). These authors have shown the influence of mesoscale activity (eddies) in the properties of the DSOW, demonstrating too that these property changes can be tracked along its path. This mesoscale variability can be seen in the isopycnal vertical displacements influenced mostly by temperature changes, but also in the vertical structure of the velocity field ([Von Appen et al., 2017](#)). These authors have proposed that this variability's source is closely linked to the propagation of eddies along the interface between the DSOW and the ambient water.

The interface dividing the DSOW and the ambient waters has been defined as the isopycnal  $\sigma_0 = 27.8 \text{ kg/m}^3$  ([Dickson & Brown, 1994](#)), which is considered to be the location for the maximum vertical density gradient. This pycnocline is confined close to the bottom at depths between 300 and 2000 meters, depending on the bathymetry ([Girton & Sanford, 2003](#)). Below this density threshold we encounter the dense overflow water plume and above it we find ambient waters with different origins depending on the location and circulation patterns (mainly IC and EGC). The relative movement of these water masses distributed vertically is also well differentiated in speed and direction, making most of the times the isopycnal  $27.8 \text{ kg/m}^3$  coincide with the maximum vertical gradient ([Macrander et al., 2007](#); [Von Appen et al., 2017](#)). Stratification and vertical shear interact in a dynamic balance, where stratification—driven by an increasing density gradient—acts to stabilize the system, while vertical shear, associated with an increasing velocity gradient, promotes mixing along the main isopycnal.

The characterization of the mesoscale variability downstream the sill at the position  $65^\circ 27.6' \text{N}$ ,  $29^\circ 19.2' \text{W}$  is one of the main objects of study of this master thesis. As well as unveiling their possible connections to the underlaying entrainment and mixing events in this region (due to

vertical shear overcoming stratification). Specifically, shedding light on the interactions between the DSOW and the ambient water above it by trying to answer the following questions:

- What are the possible sources of the mesoscale variability observed?
- Does this variability impact the changes of vertical structure?
- Can this mesoscale variability influence the development of vertical shear instabilities and promote vertical mixing?

## 2. Data

The data used in this study was obtained from high temporal resolution moorings deployed and recovered downstream the Denmark Strait by the oceanographic cruise MSM76 (Maria S. Merian) during its campaign in August 2018 ([Kanzow et al., 2018](#)). The moorings were allocated on the continental slope north-east of Greenland, southwest of the Denmark Strait, as depicted in [figure 1](#). The moorings collected data for 11 days (from August 14th to August 25th) around the depths of maximum vertical gradient. The objective of these mooring deployments was to capture the mesoscale variability of the pycnocline  $27.8 \text{ kg/m}^3$  (upper limit of the DSOW), as well as high frequency signals that could indicate the presence of vertical mixing events.

In this study I centered my analysis on the mooring DS-C-18 ([figure 2](#)), the deepest one located at a mean depth of 1145.5 meters and with coordinates  $65^\circ 27.6' \text{N}$ ,  $29^\circ 19.2' \text{W}$ . The 26 measuring devices were vertically distributed with a separation of around 10 meters space between them starting at a mean depth of 840 meters to 1100 meters. The devices were mainly composed of temperature recorders, but also together with 3 velocimeters and 2 Conductivity, Temperature,

Depth (CTD) recorders. The mean vertical positions of the velocimeters and CTDs can be seen in figure 2-a.

The main details and specifications of each measuring device have been compiled in [table 1](#).

This is a raw open-source data set and for further details about the moorings and their specifications the reader can be directed to [\(Von Appen, 2019\)](#). In this Pangaea website the reader can find the raw data, protocols, and the scheme of the mooring used for this study.

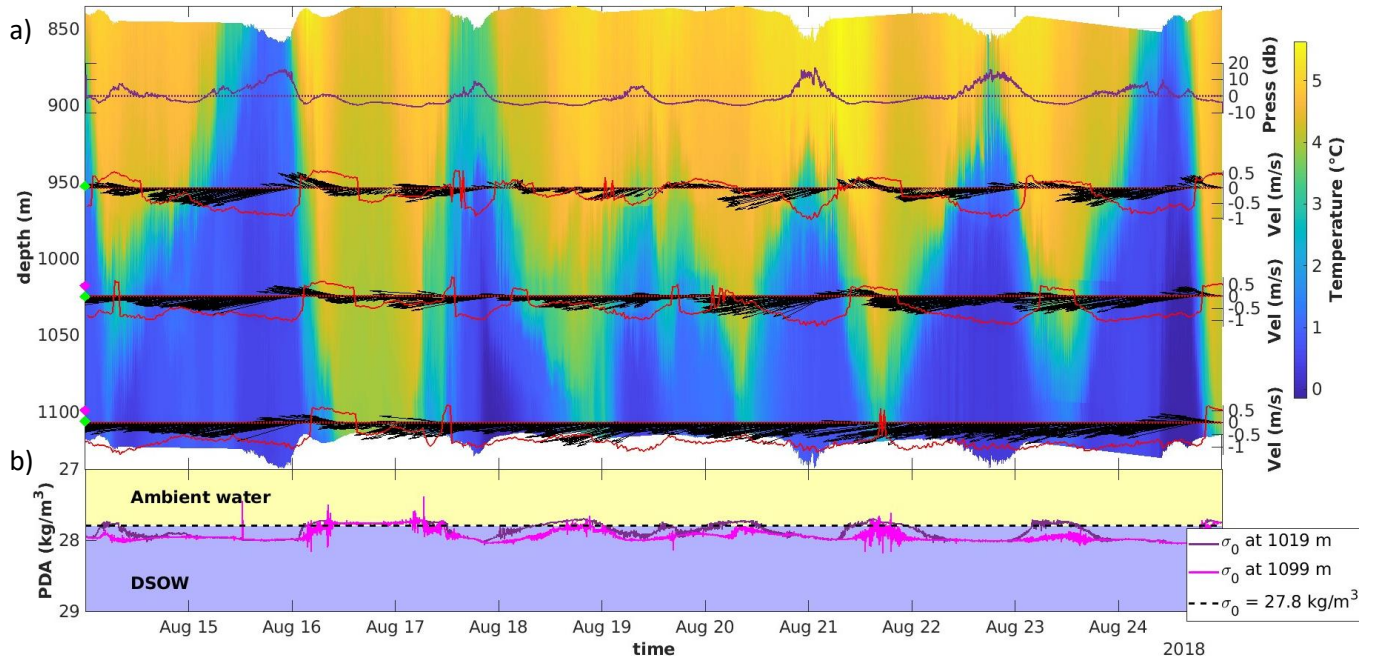


**Figure 2.** Data used in this study from the mooring DS-C-18 deployed and recovered by the MSM76 oceanographic campaign. (a) Temperature (background); velocity quiver plots from the three velocimeters (mean depth of the velocimeters is indicated by the green rhombuses); and mean pressure anomaly data (purple curve). (b) Potential density anomalies with reference to the sea surface at the two CTD positions (the CTD positions are indicated with magenta rhombuses in [figure 2-a](#)). The dashed line in (b) marks the interface layer (pycnocline  $27.8 \text{ kg/m}^3$ ) that separates the DSOW from the ambient waters.

**Table 1.** Devices' main specifications: velocimeters (2<sup>nd</sup> column); temperature recorders (3<sup>rd</sup> column); CTD recorders (4<sup>th</sup> column). Source:

Device name	Nortek Aquadopp	Seabird electronics 56	Microcat - Seabird electronics 37
<b>Sensors</b>	3D velocity, conductivity, temperature	Temperature	Temperature, conductivity, pressure
<b>Measurement interval (s)</b>	60	10	20
<b>Vertical vel. precision (cm/s)</b>	±1.4	-	-
<b>Horizontal vel. precision (cm/s)</b>	±0.9	-	-
<b>Temperature Precision (°C)</b>	±0.0001	±0.0001	±0.0001
<b>Conductivity Precision (S/m)</b>	-	-	±0.00004
<b>Pressure precision (dbar)</b>	±0.058	-	±0.058

### 3. Methodology

This study applies a combination of data processing, statistical analysis, and visualization techniques to characterize the temporal and spatial variability of the Denmark Strait Overflow Water (DSOW) and its interaction with the overlaying ambient water. The methodology ensures consistent data resolution, identifies key physical boundaries, and examines the stability and variability of the flow, providing insights into the underlying mesoscale processes.

#### 3.1. Preprocessing

Due to the differences in the measurement intervals of our 3 kinds of devices, specified in section 2, a sub-sampling via linear interpolation has been applied to the CTDs and temperature recorders to match the time resolution of the velocimeters (1 measurement per minute). Linear

interpolation was chosen instead of time averaging to match the exact times recorded by the velocimeters and to preserve the continuity of the data.

### 3.2. Definition of a reference interface layer

The first step of our analysis starts by defining a reference interface layer ( $L_R$ ) between the DSOW and the ambient water above. Due to the lack of pressure and conductivity measurements in most of the fraction of the water column observed, I have defined this interface layer as the depth of the maximum vertical temperature gradient (Eq. 1).

From the vertical temperature gradient ( $\frac{\partial T}{\partial z}$ ), I obtained the maximum value at each time step and determined its vertical position in the water column (z). The result is an interface layer that divides the DSOW from the warmer ambient water above. This layer is an estimation of the main pycnocline  $27.8 \text{ kg/m}^3$  mentioned in the previous sections.

$$L_R = z \left( \max \left( \frac{\partial T}{\partial z} \right) \right) \quad (\text{Eq. 1})$$

Where  $L_R$  is the reference interface layer defined as the depth of maximum vertical temperature gradient,  $z$  is the water depth, and  $\frac{\partial T}{\partial z}$  is the vertical temperature gradient.

The use of the temperature gradient to estimate the main pycnocline in this region is justified in previous studies ([Voet & Quadfasel, 2010](#); [Koszalka et al., 2017](#)). Where the authors state that “the density variations depend only on temperature in a first approximation”. Therefore, we can say that the density gradients are likely associated with temperature gradients. This simplifies the relationship:  $\Delta\rho \approx f(T)$  (where salinity’s role is minimal in this case). Thus, from now on our pycnocline  $27.8 \text{ kg/m}^3$  is approximated by this main thermocline that defines our  $L_R$ .

To obtain the  $L_R$  we interpolated vertically (linear interpolation) the temperature data into a finer grid. We used a grid with a 3m vertical spacing for a higher resolution of the  $L_R$ . Additionally, to remove high frequency variations, we have smoothed the  $L_R$  using a moving average of 3h. This gives us a smoother curve fitting in the region of maximum temperature gradient but filtering out the frequency variations higher than  $3h^{-1}$ . The reason for this smoothing is to have a clearer interface that highlights the low frequency variations we are interested in.

### 3.3. Rotation of velocities

For the proper characterization of the horizontal velocity field recorded by the velocimeters it is useful to transform the geo-referenced coordinate system into a coordinate system following the mean direction of the current ( $\theta$ ). Thus, the X-axis is rotated to be positive towards the mean direction of our flow and the Y-axis perpendicular to it. In this way, we can divide the velocity components into the along-stream velocity ( $u_a$ ) and the cross-stream velocity ( $u_c$ ).

We part from the original geo-referenced horizontal velocity field  $V_h = u_N + u_E$ , where  $u_N$  and  $u_E$  represent the northwards and eastwards velocities respectively.

Then, the  $\theta$  is obtained for each velocimeter by using the atan2 function for the mean northwards and eastwards velocities in the following way:

$$\theta = \text{atan} 2 (\overline{u_E}, \overline{u_N}) \quad (\text{Eq. 2})$$

Where  $\theta$  is the mean direction of the current,  $u_E$  is the eastward velocity component, and  $u_N$  is the northward velocity component.

Once  $\theta$  is obtained we can rotate  $V_h$  by applying the trigonometric functions:

$$u_a = u_E \cos \theta + u_N \sin \theta \quad (\text{Eq. 3})$$

$$u_c = -u_E \sin \theta + u_N \sin \theta$$

Where  $u_a$  is the along-stream velocity component, and  $u_c$  is the cross-stream velocity component.

The resulting coordinate system is therefore rotated clockwise from the original cardinal system by  $\theta$  degrees as shown in [figure 3](#).

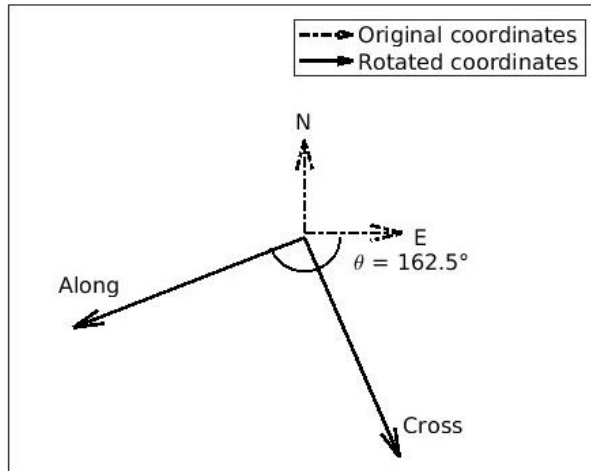


**Figure 3.** Scheme of rotation for middle velocimeter. The new coordinate system is rotated clockwise towards the mean direction of the current (Along) for the middle velocimeter by an angle  $\theta = 162.5^\circ$ .

### 3.4. Power spectral density (PSD) estimation

The estimation of the Power Spectral Density (PSD) has been used to study the degree of influence of the mesoscale variability in our velocity, temperature and salinity data. This estimation decomposes the signal into its constituent frequencies, each associated with a specific amplitude. This analysis enables the identification of dominant frequencies that contribute most significantly to the variability observed in the data, providing insights into the scales and magnitudes of underlying physical processes.

The resulting PSD provides a detailed representation of the signal's frequency content. Peaks in the PSD indicate frequencies at which the signal exhibits relatively higher energy, corresponding

to the dominant modes of variability. These peaks are linked to specific periods or timescales of variability and are analyzed to identify the physical phenomena influencing the measured data.

To estimate the PSD, the Multitaper Method ([Thomson, 1982](#)) is employed. This method is particularly well-suited for spectral analysis because it minimizes spectral leakage while providing a robust and high-resolution estimate of the PSD.

From the PSD we can also quantitatively estimate the percentage of contribution of each peak to the total variance of our distributions. In this way we can estimate the contributions of the different peaks to the total variance of the signals with the formula:

$$Pv = \frac{\int_{f-\Delta f}^{f+\Delta f} PSD(f) df}{\int_{-\infty}^{+\infty} PSD(f) df} \times 100 \quad (Eq. 4)$$

Where Pv is the percentage of variance explained, PSD is the estimated power spectral density, f is the frequency of interest, and  $\Delta f$  is the frequency window around f.

We used this equation to estimate the percentage of variance explained by the mesoscale phenomena or low frequency variations. We also estimate for comparison the percentage of variance explained by the tidal peaks.

### 3.5. Wavelet analysis

In this study, wavelet analysis was applied to analyze the flow's velocity components and temperature and salinity measurements. The technique provided insight into the temporal variability of the signal's frequency content, revealing how the power of the different frequency components is distributed in time. The wavelet analysis produces time-frequency maps

(scalograms) used to qualitatively identify how the dominant frequency peaks are distributed in time, and to investigate the potential relationships across different frequency bands.

The wavelet transform was performed using the continuous wavelet transform (CWT), which is ideal for studying time-series data with varying periodicities. For this project we used the CWT implementation available in the literature ([Lilly, 2024](#)). For the wavelet parameters, we used gamma = 3 and beta = 3, as these values offer a balance between time and frequency resolution, making them well-suited for capturing both sharp transients and smoother periodic components in the data. Near the edges of the signal, there is less data to convolve with the wavelet, which leads to distortions or inaccuracies. The cone of influence (COI) in wavelet analysis is a region on the scalogram that indicates where edge effects become significant, and the results may be less reliable.

### 3.6. Cumulative vector diagram

The use of this plotting technique gives us an idea of the path followed by the currents passing through the mooring. It gives us the displacement of the water if it was advected by the currents at the measuring point. To build this graph we must first compute the displacement between each velocity observation to the next one ( $X = V \cdot dt$ ). The next step is to make a cumulative sum of the calculated displacements with increasing time step. This procedure can be mathematically described in the following form:

$$S_k = \sum_{i=1}^k X_0 + V_k dt \quad (Eq. 5)$$

Where  $S_k$  is the cumulative displacement vector at time step ‘k’ ( $S_k = [S_{xk}, S_{yk}]$ ),  $X_0$  in the initial computed displacement ( $X_0 = [x_0, y_0]$ ),  $V_k$  is the velocity at time step ‘k’, and  $dt$  is the time resolution of the data.

In this way we construct for both components ( $u_a$  &  $u_c$ ) the displacement of a particle passing through our mooring, where the initial point is  $S_{k=0} = X_0 = [x_0, y_0]$  and the end point is  $S_{k=end} = [S_{xk=end}, S_{yk=end}]$ .

### 3.7. Polar hodograph

The polar hodograph is a qualitative technique that was used to analyze velocity anomalies representing the background flow in polar coordinates. The first step in this process is to calculate the absolute velocity at each time step, which is represented as the radial distance in the hodograph. Each velocity observation is then assigned an angular orientation relative to true north, allowing the flow's changing direction to be visualized in the cardinal plane.

To reduce the impact of high-frequency fluctuations, a time-averaging method is applied with a 1-hour averaging window. This smoothing technique helps eliminate sub-hourly fluctuations to focus on the velocity variabilities above 1h. By examining the smoothed data, we can determine the rotational characteristics of the flow. The direction of rotation—whether cyclonic (counterclockwise) or anticyclonic (clockwise)—can be inferred based on the orientation and movement of the velocity anomalies in the polar hodograph.

This method provides a clearer understanding of the flow behavior, enabling the identification of underlying patterns and larger-scale rotational features. The polar hodograph thus serves as a tool for assessing the nature of the flow, and its response to different time scales forcing factors.

### 3.8. Richardson number

The final step of my thesis is studying the interactions between the DSOW and the ambient water above it. To do so we used the CTDs and velocimeters to analyze the vertical structure of our recorded water column. From the CTDs we can derive the vertical stratification between the two depths of our CTDs and from the velocimeters we derive the vertical shear between them.

In oceanography the measure of the vertical structure mainly depends on the density and velocity fields. The density vertical structure is often measured with the so-called Brunt–Väisälä frequency ( $N^2$ ), denoted by:

$$N^2 = \frac{-g}{\rho} \frac{\partial \rho}{\partial z} \quad (\text{Eq. 6})$$

Where  $N^2$  is the Brunt–Väisälä frequency,  $g$  is gravity,  $\rho$  is the density of the water, and  $z$  is the water depth.

Whereas the velocity vertical structure is measured by the vertical shear ( $Sh$ ), denoted by:

$$Sh = \sqrt{\left(\frac{\partial u_a}{\partial z}\right)^2 + \left(\frac{\partial u_c}{\partial z}\right)^2} \quad (\text{Eq. 7})$$

Where  $Sh$  is the vertical shear.

These two properties of the water column give us information about its stability. A high  $N^2$  means vertical stability (stratification) of the water column and vice versa. On the contrary, a high vertical shear means low vertical stability of the water column and vice versa. Both magnitudes interact with each other giving us the overall vertical stability of the water column. One important measure of the water column stability is therefore derived from their interaction, the Richardson number. This non-dimensional number represents the ratio of  $N^2$  and  $Sh$  as:

$$Ri = \frac{N^2}{|Sh|^2} \quad (Eq. 8)$$

Where Ri is the Richardson number.

The threshold for stability/instability is given by  $Ri = 1/4$  ([Olbers & Eden, 2012](#)). Where  $Ri < 1/4$  is the necessary condition for instability and  $Ri > 1/4$  indicates a vertically stable water column. In this study we disregard the negative values of the Ri, indicating the presence of negative  $N^2$  (buoyancy instabilities). Only one negative value in  $N^2$  was detected on late August 15<sup>th</sup>, which is not sufficient data to be object of study.

To make these calculations possible we have interpolated vertically (linear interpolation) the velocity and density data into a common grid of 5m vertical step. Then we calculated the vertical structure ( $N^2$ , Sh and Ri) from the interpolated layers at the mean depth between the two CTDs positions.

## 4. Results

This study aims to characterize the way the DSOW interacts with the lighter ambient water above it and shed light on the sources of variability of these water masses. For that we need first to define the limit between these two water masses so we can study their properties separately. The second step is to decompose the frequencies of our temperature and velocity signals to quantify their influence on the total variance and estimate their scales, as well as looking for potential interactions between low- and high-frequency components. The third step is to characterize the relative movement of these water masses to understand which phenomenon could be causing the observed variability. Finally, we take a closer look into the interactions

between these two water masses by deriving the vertical structure and searching for vertical shear instabilities situations.

Please note that for illustration I have used in [sections 1-4](#) the velocity and temperature data from the middle velocimeter (mean depth = 1040m). I have selected this device since it is the most centered in the region of maximum variability as we can visually deduce from [figure 2-a](#). In the same way I have used for the wavelet analysis the temperature and salinity data from the CTD right above this velocimeter, that is at a mean depth of 1030m. For the complete velocity and temperature analysis the reader can be directed to [Supplementary figures](#).

#### 4.1. Division of water masses

First, we want to divide our time series into two different regimes: (a) fast and cold deep waters (DSOW) and (b) slow and light waters (ambient water). To do so we use the definition of the  $L_R$  given in [section 3.2](#). to build this reference interface layer dividing the two different regimes, as shown in [figure 4](#). We can observe that the  $L_R$  fits with the depths at which we encounter the transition between warm and cold waters. This is the depth of maximum vertical gradient in temperature. The only times where the  $L_R$  does not fit the shape of the temperature map are in the exact times when any of the water masses is not vertically present. That is during late August 15<sup>th</sup>, when the DSOW covers the whole recorded water column; and late August 16<sup>th</sup>, when the DSOW falls below our deepest temperature recorder.

The velocity components for the different regimes are displayed in [figure 4-b & 4-c](#), where we can distinguish the clear alternating patterns from fast to slow motions in the  $u_a$  component ([figure 4-b](#)) whether our device is located above or below the  $L_R$ , respectively. Alongside, the  $u_c$  component, [figure 4-c](#), has too recognizable alternating patterns, changing from a more high-

frequency dominated regime (DSOW) oscillating around  $u_c = 0$ , and a smoother regime (ambient water) dominated by a first negative shift in the  $u_c$  (towards Greenland) which is followed by a later less pronounced positive displacement (towards Iceland).

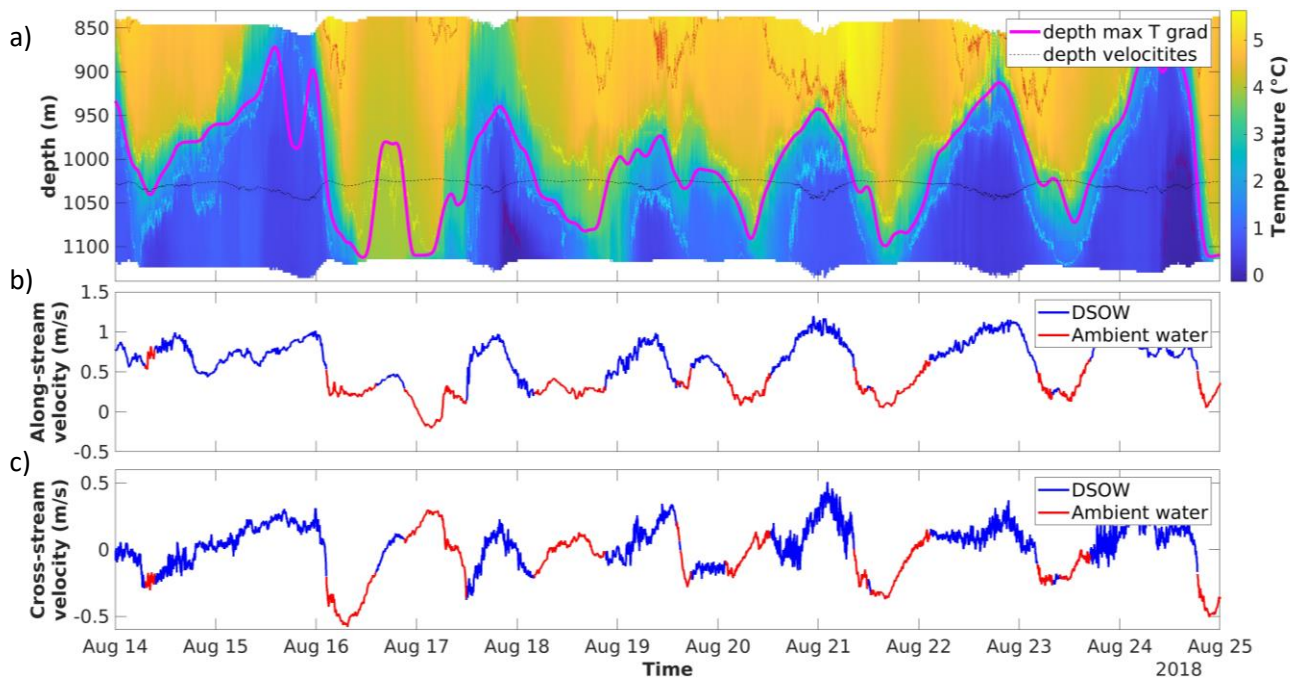


**Figure 4.** Division of DSOW and ambient water. (a) Water temperature with contours [0, 1, 4, 5] °C with respective colors [purple, cyan, yellow, red], and estimated pycnocline 27.8 kg/m<sup>3</sup> (magenta line) using the maximum vertical temperature gradient ( $L_R$ ). The dashed black line represents the depth of the middle velocimeter. (b & c) Rotated horizontal velocity components ( $u_a$  &  $u_c$  respectively) at the middle velocimeter (mean depth = 1040m) divided by waters above the  $L_R$  (red) and waters below the  $L_R$  (blue).

The  $L_R$  lies predominantly in between the 1°C and the 4°C isotherms, which means that these isotherms represent the limits for the maximum vertical temperature gradient. The mean temperature along the  $L_R$  is 2.6°C. Furthermore, the mean depth of the derived  $L_R$  has been

estimated to be 1002.5m with a standard deviation of  $\pm 67.4$  m. This means that the total vertical displacement of our  $L_R$  seems to be of the order of 10-100 meters.

The constructed interface layer allows us to analyze separately the physical properties of the two different regimes and compare them. Above the  $L_R$  we encounter ambient water and below it the DSOW. In this way, we have calculated their mean physical properties with their respective standard deviations to build [table 2](#).

**Table 2.** Computed means (standard deviation) for the two regimes: DSOW and ambient water.

	$u_a$ (m/s)	$u_c$ (m/s)	velocity magnitude (m/s)	direction (°)	temperature (°C)	salinity (‰)
<b>DSOW</b>	0.75 ( $\pm 0.20$ )	0.07 ( $\pm 0.14$ )	0.75 ( $\pm 0.24$ )	152.1 ( $\pm 1.54$ )	1.20 ( $\pm 0.98$ )	34.82 ( $\pm 0.03$ )
<b>Ambient water</b>	0.27 ( $\pm 0.18$ )	-0.12 ( $\pm 0.20$ )	0.28 ( $\pm 0.26$ )	172.9 ( $\pm 1.13$ )	4.10 ( $\pm 0.96$ )	34.92 ( $\pm 0.04$ )

The resulting means and standard deviations give us insight into the different nature of the two water masses identified. Below the  $L_R$  we find a faster colder and fresher water, the DSOW, with a dominant  $u_a$  component. Above the  $L_R$  we find a slower warmer and saltier water, ambient water, with a shifted current direction by  $20.8^\circ$  towards Greenland (westwards).

From [table 2](#) we have derived and plotted the mean direction and magnitude of the velocities of both water masses in [figure 5](#). The direction of propagation of the DSOW seems to be parallel to the isobaths, which is one of the properties inherent to gravity-driven currents. On the other hand, the ambient waters have a mean propagation direction shifted to the West, across the isobaths.

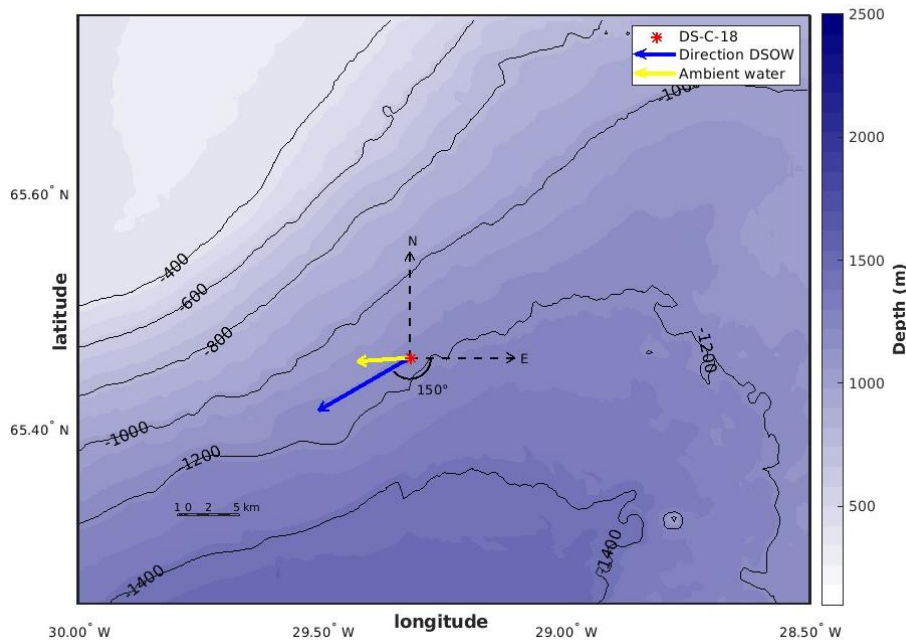


**Figure 5.** Bathymetry and mean direction and magnitude of the flow below the pycnocline (DSOW) and above it (ambient water). Derived from [table 2](#).

## 4.2. Spectral Analysis

In order to obtain the periods of maximum variability we must decompose the velocity and temperature signals into the whole range of frequencies through the estimation of their PSD, as described in [section 3.4](#).

Two main peaks can be observed in [figure 6-a](#) for both velocity components, one probably associated to the diurnal tides (around 1 cycles/day) and the other associated to low frequencies at the frequency interval  $[0.44, 0.74]$  days $^{-1}$ , with its maximum at 0.54 days $^{-1}$  (period = 1.8-days). On the other hand, when looking at the temperature PSD in [figure 6-b](#) only the low frequency peak (1.8-days period) stands out in the temperature signal whose strength decays away from the region of maximum variability in both directions (up and down in the water column). It is therefore possible to deduce that the temperature variability near the region of maximum vertical

temperature gradient is tightly linked to these low frequency events, whereas away from the vertical gradient this effect becomes less and less pronounced.

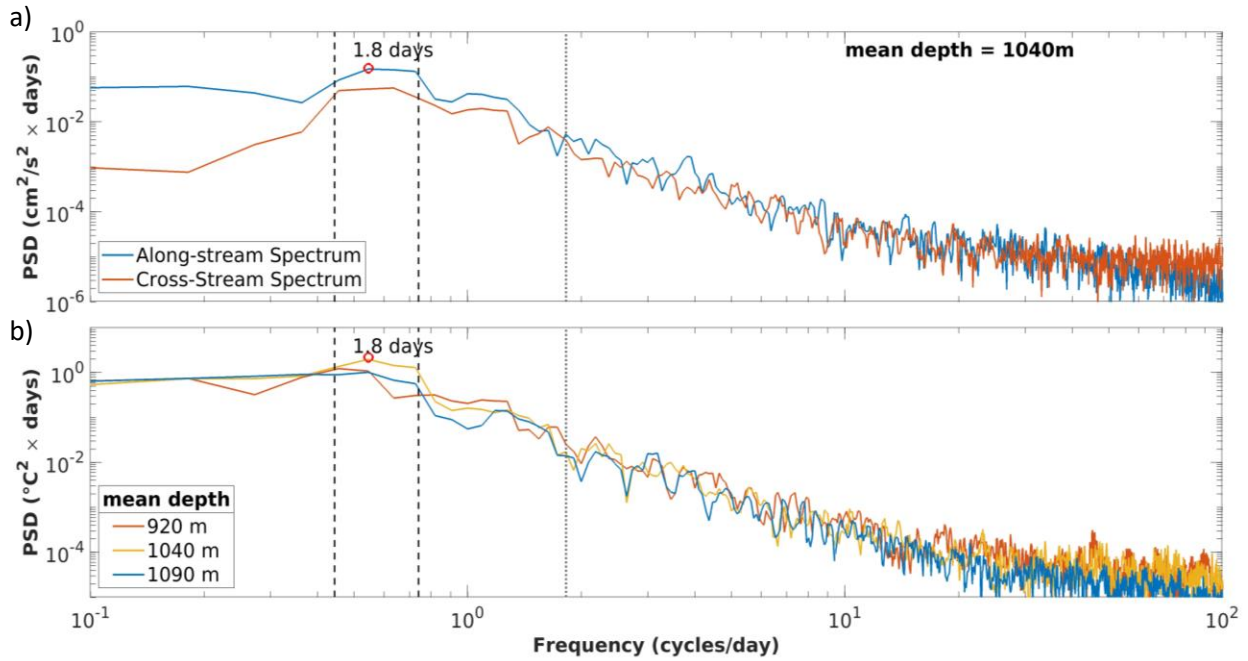


**Figure 6.** Power spectral density estimations of (a) rotated horizontal velocity components from middle velocimeter (mean depth = 1040 m); and (b) temperature data above (red), centered (yellow) and below (blue) the region of maximum variability. The dotted grey line represents the Coriolis frequency, and the two dashed black lines denote the interval of impact of the mesoscale variability [0.44, 0.74] days $^{-1}$  around the 0.54 days $^{-1}$  peak ( $T = 1.8$  days).

It is also observable in figure 6-a that while the  $u_a$  component dominates the high frequencies, the  $u_c$  seems to dominate the low frequencies. This indicates that the larger fluctuations are associated with changes in the  $u_a$  and the smaller ones are associated with changes in the  $u_c$ .

The low frequency peak ( $0.54$  days $^{-1}$ ) is therefore our feature of interest and focus of this study: the 1.8-days period peak. We can say that these events have a mesoscale size for the given

latitude, since their frequency is approximately double of the inertial frequency for this region ( $0.54 \text{ days}^{-1} < f_{\text{inertial}} = 1.82 \text{ days}^{-1}$ ).

Now we can make use of [Eq. 4](#) to estimate the percentage of variance that is explained by those peaks. For the velocity spectra the contribution of the diurnal peak ( $f = 1.09 \text{ days}^{-1}$ ) to the variance is 17.47% while the contribution of the 1.8-day period ( $f = 0.54 \text{ days}^{-1}$ ) explains 48.33% of the total variance (both with a frequency window,  $\Delta f$ , of 0.2 cycles/day). Whereas in temperature the same diurnal peak represents just 6.17% and the 1.8-day peak 50.69% of the temperature variability. This suggests that this mesoscale variability alone explains around 50% of the total variability of the velocity and temperature data.

The horizontal scale of these mesoscale events can be also estimated by using this 1.8-day peak frequency together with the means obtained in [table 2](#). To estimate the horizontal scale, I used the mean velocities of the DSOW and ambient water and multiplied by the 1.8-day period. The obtained scales can be seen in [table 3](#).

**Table 3.** Computed mean horizontal scale of the regimes: DSOW and ambient water.

	Along-stream displacement (km)	Cross-stream displacement (km)	Magnitude of displacement (km)
<b>DSOW</b>	~ 116.64	~ 10.10	~ 117.08
<b>Ambient water</b>	~ 42.00	~ -18.66	~ 45.96

The mesoscale horizontal displacements estimated above suggest that the horizontal size of the warm water events during the depression of the pycnoclines is about half of the size of the cold water events during the uplift of the pycnoclines. This would mean that in space the fluctuations have horizontal asymmetry, resulting in spatially skewed isopycnals respect time.

Now, to observe how these frequencies are distributed in time we can make use of the wavelet analysis (section 3.5), which not only shows us the times of maximum variability and their relative strength but also shows possible connections between the low- and high-frequency events. For instance, figure 7 shows a stronger impact of the low frequencies in the  $u_a$  part than in the  $u_c$  part. On the contrary, the  $u_c$  seems to dominate the high frequency part of the spectrum (figure 7-c). It is interesting to note that the mesoscale events in figure 7-b and the high-frequency events in figure 7-c seem to exhibit a temporal connection. In concrete, high frequency events seem to take place during the sloping of the  $u_a$  component.

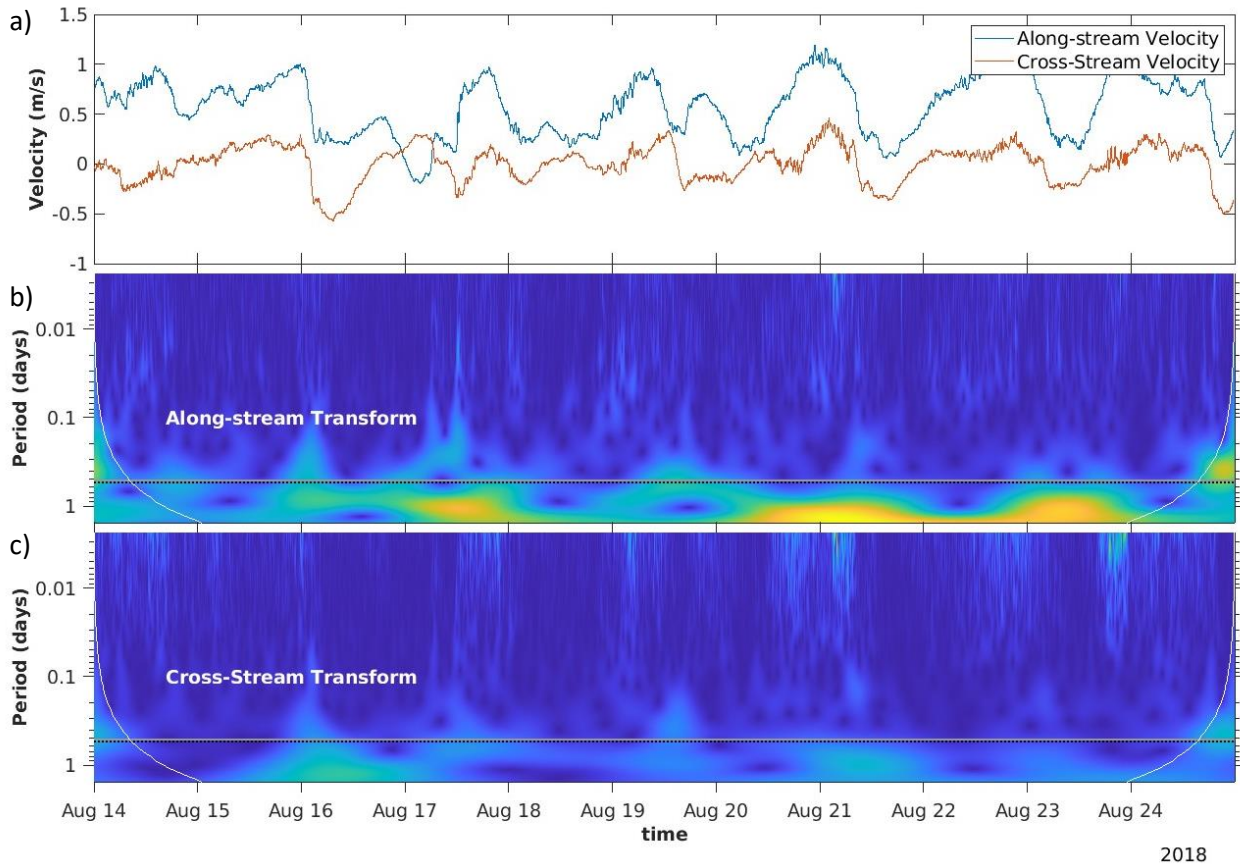


**Figure 7.** Wavelets analysis of velocities (mean depth = 1040m). (a) Velocity components over time. (b) Along-stream wavelet transformation. (c) Cross-stream velocity transformation.

In the same way, figure 8 shows the decomposed temperature and salinity frequencies from the shallowest CTD recorder (mean depth = 1030m) distributed in time. I have incorporated the wavelet of the salinity measurements to investigate its differences with respect to the temperature. In general salinity measurements follow quite well the temperature time series. However, some differences are detectable such as on the days 14<sup>th</sup>, 16<sup>th</sup>, 18<sup>th</sup> and from 19<sup>th</sup>-20<sup>th</sup>, when the salinity time series significantly drops or does not follow the temperature distribution. Moreover, the salinity frequency distribution seems to have shifted towards higher frequencies with respect to the temperature.

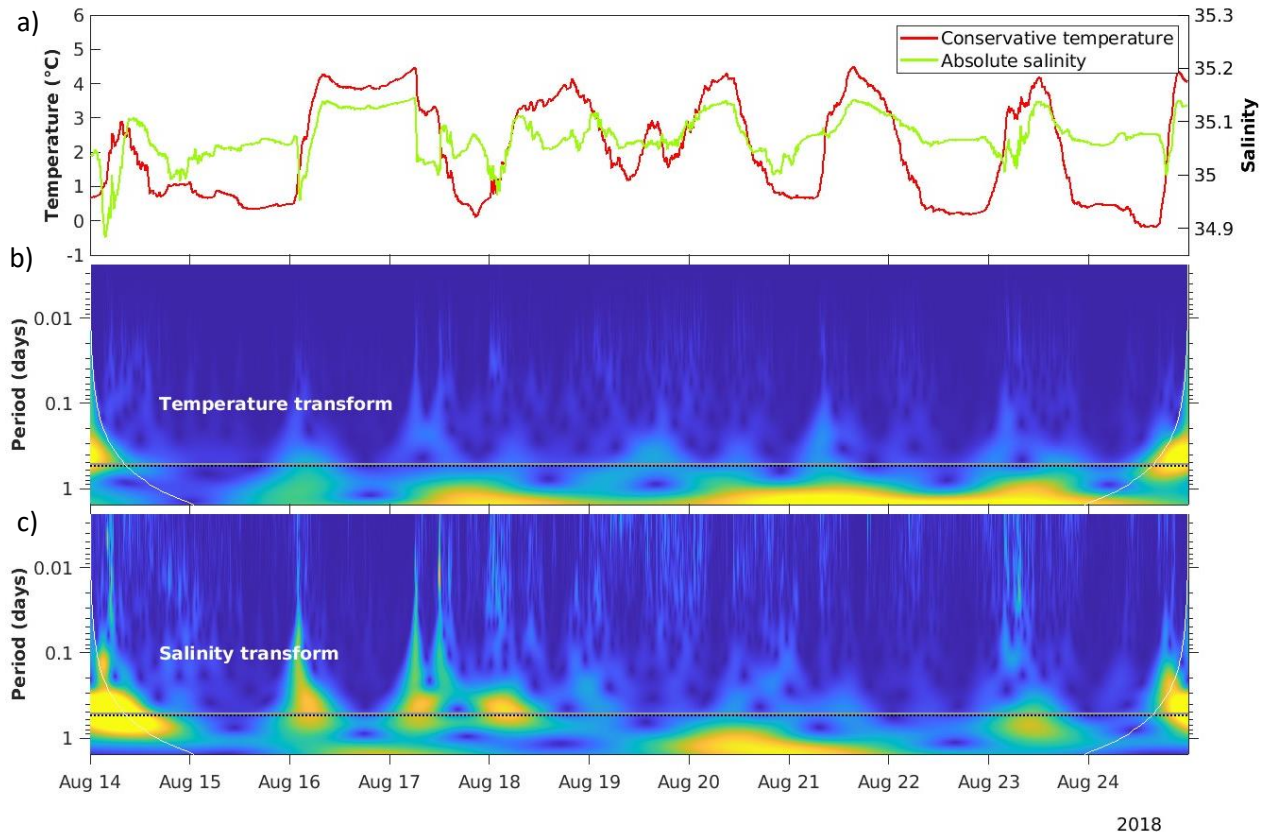


**Figure 8.** Wavelets analysis of temperature and velocity (mean depth = 1030m). (a) Conservative temperature and absolute salinity over time. (b) Conservative temperature wavelet transformation. (c) Absolute salinity wavelet transformation.

### 4.3. Mesoscale characterization

The techniques we have used to characterize the flow of the observed mesoscale activity are the cumulative vector diagram and polar hodograph explained in [section 3.6](#) and [section 3.7](#), respectively. From summing up the cumulative displacement at each time-step we obtain [figure 9-a](#), here we see how warm and cold waters have opposite relative displacements with respect to the mean direction of the flow,  $\theta$ .

During warm water events velocities are shifted clockwise from  $\theta$  and during cold water events counterclockwise from  $\theta$ . We can also distinguish the above discussed stronger cross-stream displacement during the warm water events being almost perpendicular to the along-stream displacements towards Greenland. During the whole period the vector displacements seem to follow a similar behavior, except for the second warm water and subsequent cold water events (along stream displacements from 150-200 km). This event corresponds to the period from 16<sup>th</sup> to 17<sup>th</sup> of August (mentioned in [section 4.1.](#)), when the ambient water occupies vertically the recorded water column. These punctual behaviors could have been influenced by the anomalous increase in strength of these kinds of events, also reflected in the increased slope of the isotherms (and thus the  $L_R$ ), reflected in [figure 4](#), during this period.

Furthermore, the ratio of the horizontal scales derived in [table 3](#) seem to match well with the derived horizontal displacements in [figure 9-a](#). Cold water events show a bigger total horizontal displacement, around double the size of the warm water events. However, the magnitudes derived are slightly superior to the observed ones in the cumulative vector displacement diagram. This difference can be explained by smaller scale processes overlapping the mesoscale events.

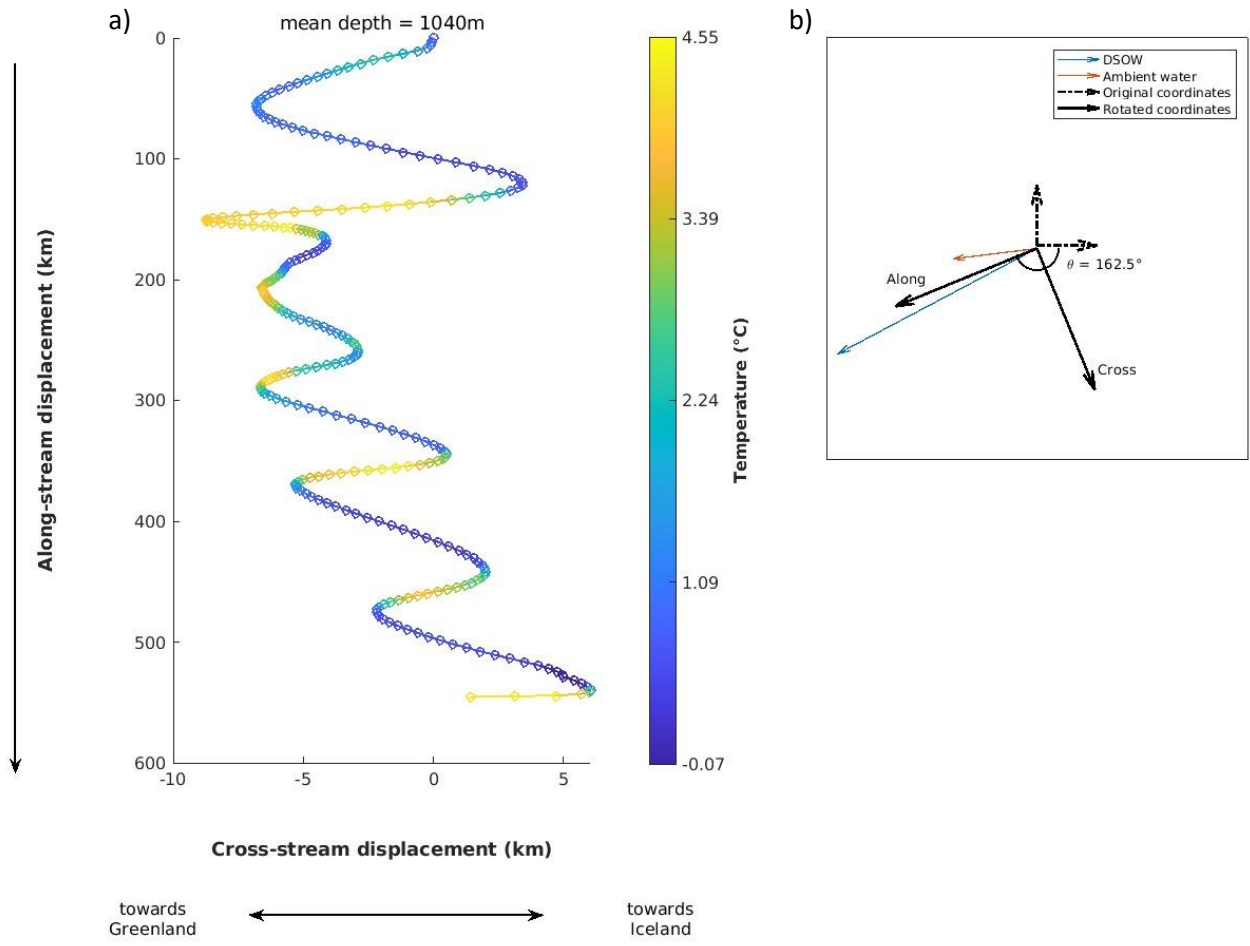


**Figure 9.** (a) Cumulative vector displacement diagram derived from the rotated velocity data from the middle velocimeter (mean depth = 1040m) colored with its respective temperatures. (b) Scheme of coordinates rotation. The blue and red lines represent the mean direction and magnitude of the DSOW and the ambient water, respectively.

A closer inspection can be done by zooming in into these events and computing the velocity anomalies as presented in [figure 10-11](#). These results show a clear distinct behavior during warm water and cold water events. During cold temperature events, we observe a regime with increased high-frequency variability associated with DSOW ([figure 10](#)) while during warm temperature events we observe a smoother regime ([figure 11](#)). Both regimes show a dominant rotational pattern close to the  $L_R$ . The dominant apparent rotation of the cold water events,

observed in the hodograph in figure 10-d is cyclonic, whereas the dominant rotation during warm water events observed in figure 11-d is anticyclonic. These rotational patterns resemble an eddy-like behavior, which could be an indicator of anticyclonic warm-core eddies and cyclonic cold-core eddies passing along the main pycnocline intermittently. The strength of these rotational patterns seems to decay away from the  $L_R$  (The closer the velocimeter to the  $L_R$  the stronger the rotation pattern), which indicates that these eddies travel along the main pycnocline.

All the events have been analyzed separately and all of them follow similar patterns. For the complete velocity anomaly characterization, the reader can refer to [Supplementary figures](#).

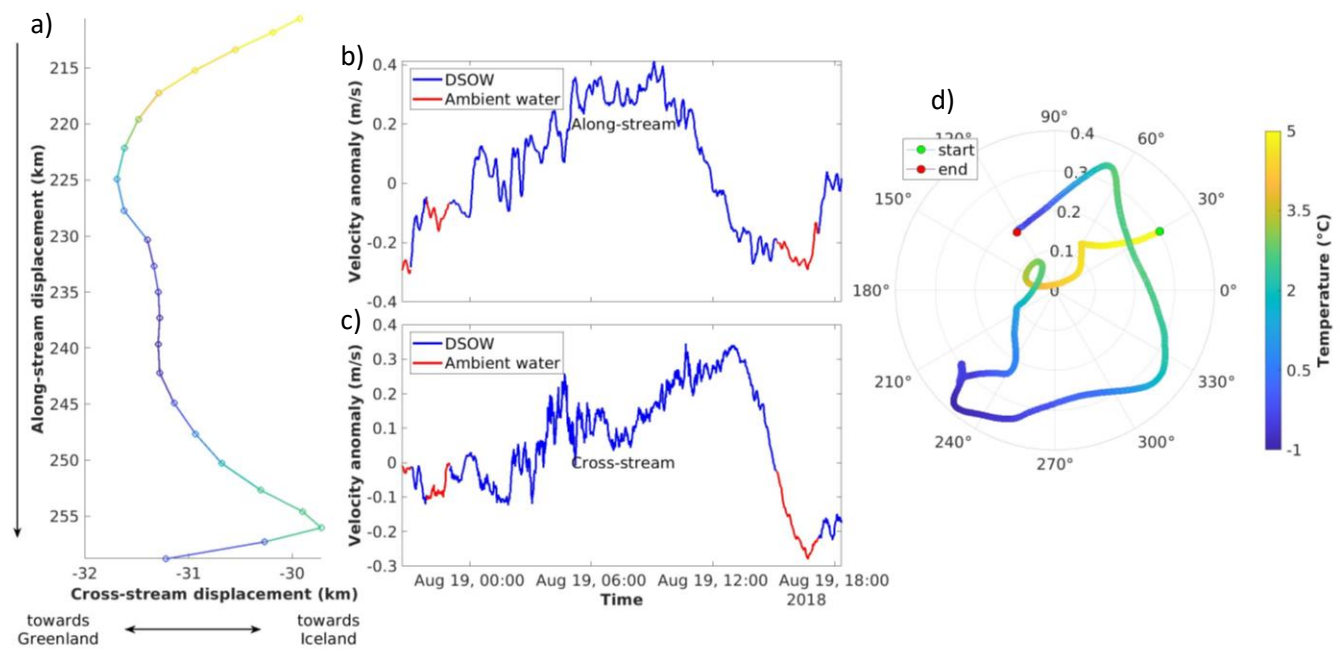


**Figure 10.** Characterization of cold mesoscale fluctuation (cyclonic) on August 19th. (a) Figure 7-b zoomed in at the time of a cold water fluctuation; (b & c) rotated velocity anomaly of  $u_a$  and  $u_c$ , respectively. (c) Polar hodograph of non-rotated velocity anomalies with temperature color.

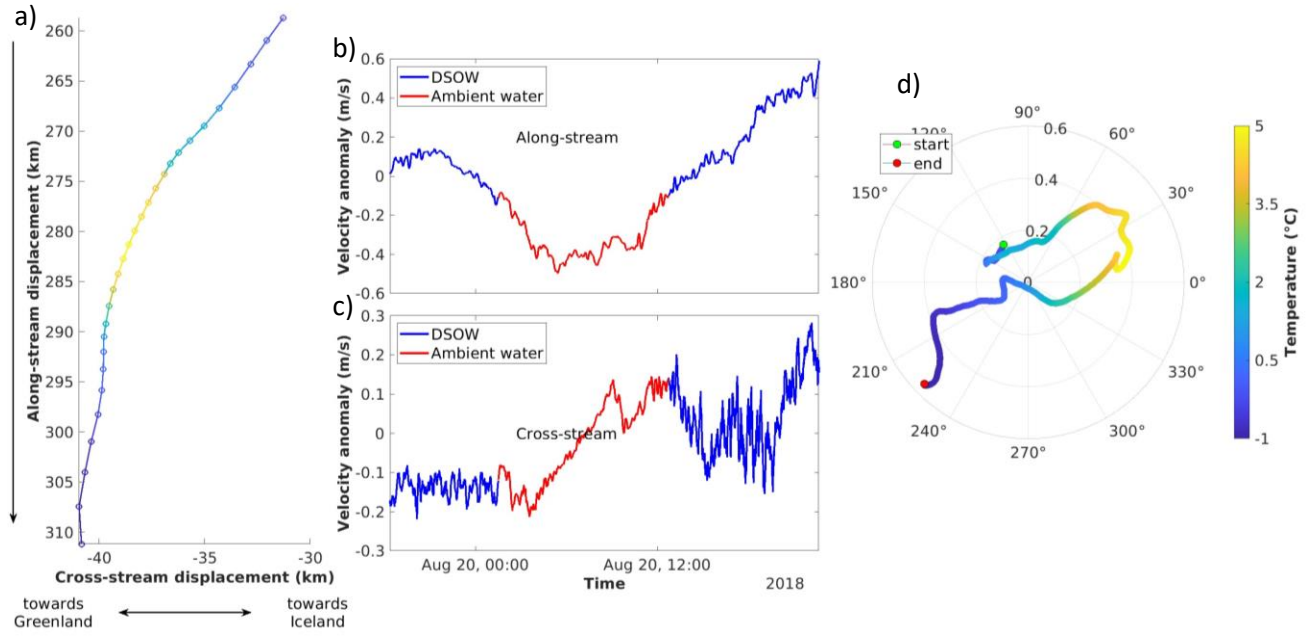


**Figure 11.** Characterization of warm mesoscale fluctuation (anticyclonic) on August 20th. (a) Figure 7-b zoomed in at the time of a warm water fluctuation; (b & c) rotated velocity anomaly of  $u_a$  and  $u_c$ , respectively. (c) Polar hodograph of non-rotated velocity anomalies with temperature color.

#### 4.4. Detection of vertical shear instabilities

The last step of our study is to investigate the vertical structure of our water column around the region of maximum temperature gradient. Particularly, I am interested in the detection of vertical shear instabilities and for that we used section 3.8. The Ri serves as an estimation of the stability of the water column comparing the magnitude of the stratification against the velocity shear.

We can observe in figure 12-a how  $N^2$  and Sh compensate for each other almost simultaneously. This is expected to happen since the depth of maximum Sh is closely linked to the depth of maximum gradient (high stratification = high  $N^2$ ). Occasionally the vertical shear overcomes stratification making it possible for vertical instabilities to develop. The graph also shows two equilibrium states of the vertical structure, a low stratified and low shear state away from the maximum gradient (in both directions) and a high stratified and high shear state close to the  $L_R$ .

Figure 12-b shows that the estimated  $Ri$  drops often below  $Ri < \frac{1}{4}$  (necessary condition for instabilities) along the mean depth between the 2 CTDs positions.

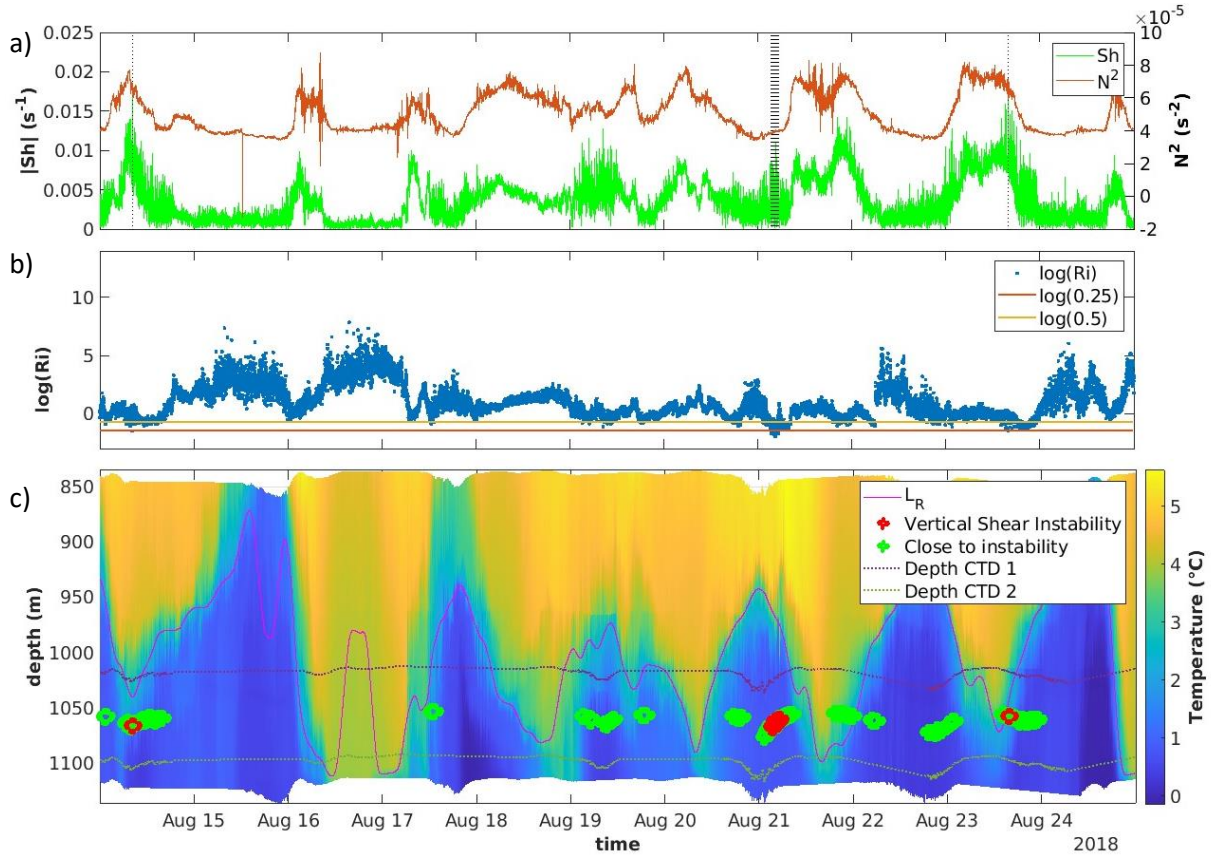


**Figure 12.** Detection of unstable and close to unstable conditions in the vertical structure between the two CTDs. (a) Measure of vertical structure ( $Sh$  and  $N^2$ ), grey doted lines show vertical shear instabilities detected. (b) Evolution of the  $Ri$  over time with two limits:  $Ri < \frac{1}{4}$  (unstable) and  $Ri < \frac{1}{2}$  (close to unstable); (c) distribution of the two previous conditions in time and at the mean depth between the two CTDs. The magenta line shows the previously defined  $L_R$ .

In addition to the instability interval  $Ri = [0, \frac{1}{4}]$ , a close to instability interval  $Ri = [\frac{1}{4}, \frac{1}{2}]$  was added to include all the relative minimums within the  $Ri$  and look for the conditions when the water column is in the limit to become unstable. These two specified conditions were scattered

over the temperature plot in figure 12-c to visualize when and where in the inferred depth (average depth of the CTDs) they happen.

We can observe how the more unstable conditions seem to happen below the  $L_R$  that is inside the DSOW layer. In fact, the detections of the instability necessary condition ( $Ri < \frac{1}{4}$ ) are only present below the  $L_R$ . It is in these moments when the  $Sh$  overcomes  $N^2$  making it possible for instabilities to develop and therefore an indicator of possible vertical mixing processes happening. This suggests that instabilities are more likely to develop when the maximum vertical shear is displaced below the  $L_R$ .

## 5. Discussion

The results of our study provide valuable insights into the dynamics of the Denmark Strait Overflow Water (DSOW) and its interaction with the surrounding ambient waters. Our findings highlight three key aspects: the distinct characteristics of DSOW and ambient water, the vertical movement of isopycnals possibly influenced by eddies, and the development of instabilities near the interface layer. These interactions and their implications are discussed below.

### 5.1 Characterization of the water masses

The data clearly distinguishes two different flow regimes: the Denmark Strait Overflow Water (DSOW) and the lighter ambient waters above it. The DSOW is identified as a colder, faster, and fresher water mass, with a strong along-stream velocity component ( $u_a$ ) and a mean propagation direction aligned with the isobaths. In contrast, the ambient waters are warmer, slower, and slightly saltier, with a mean direction that is shifted westward, across the isobaths. These

findings suggest that most part of the ambient water originates in the recirculation of the IC downstream the Denmark Strait sill into the Spill Jet, coinciding with previous findings near this area ([Von Appen et al., 2014](#))

Interestingly, during transitions between DSOW and ambient water, low salinity anomalies are occasionally recorded within the ambient water layer. These anomalies suggest that the ambient water may not be a single, homogeneous water mass but could be a composite of different water sources. Previous studies attribute these low salinity anomalies in the ambient water to be caused by the EGC ([Von Appen et al., 2014](#)). These findings highlight the complexity of the flow structure in this region and point to the need for further investigations into the origins and pathways of the ambient water masses.

## 5.2 Isopycnal Displacements

The isopycnals in this study exhibit significant vertical displacements (in the order of 10-100 meters) over time linked to mesoscale processes within a mean period of 1.8 days. The sources of these vertical displacements seem to be related to the propagation of mesoscale features such as mesoscale eddies. The evaluation of the velocity anomalies seems to reveal the consecutive propagation of cyclonic and anticyclonic eddies along the mean isopycnal ( $27.8 \text{ kg/m}^3$ ). Cyclonic eddies associated with cold water events are associated with elevation of the isopycnals, while anticyclonic warm-core eddies are associated with isopycnal depression. These opposing phenomena create a dynamic interplay that produces the observed vertical oscillations of the interface layer ( $L_R$ ). The detection of these mesoscale eddies and their effect in isopycnal displacements has been previously studied at different locations, at the Denmark Strait sill ([Moritz et al., 2019; Von Appen et al., 2017](#)), and downstream of the sill ([Voet & Quadfasel, 2010](#)). These

findings suggest that the advection of mesoscale eddies is closely linked to the isopycnal fluctuations and arise questions on how their interactions led to the observed quasi-regular periodicity of the variability in the period interval from 1.4 to 2.3 days (which has been estimated to explain about the 50% of the temperature and velocity variance).

Additionally, the horizontal asymmetry in isopycnal displacements is noteworthy. The DSOW, being faster and denser, covers a larger horizontal range compared to the slower ambient water. This asymmetry likely results in spatially skewed isopycnals, which indicates that spatially the sloping of the isopycnals is steeper than temporally.

### 5.3 Instabilities and Vertical Mixing

The interface layer ( $L_R$ ) between the DSOW and ambient waters is a critical zone for vertical shear instabilities, where Richardson number ( $Ri$ ) analysis frequently reveals unstable conditions ( $Ri < \frac{1}{4}$ ). These instabilities occur when vertical shear exceeds stratification, leading to mixing processes, particularly within the DSOW layer below the interface.

Eddy-induced isopycnal displacements could increase the likelihood of instability by causing mismatches between the depths of maximum shear and stratification. These mismatches, especially during isopycnal depressions or elevations, create conditions that promote vertical mixing and can alter flow structures and stratification over time.

Wavelet analysis of velocity components suggests that interactions between low-frequency along-stream and high-frequency cross-stream fluctuations are associated in time with these instabilities, indicating their development may be linked to interactions between low-frequency mesoscale events and high-frequency oscillations.

## 5.4 Schematics

A schematic (Figure 13) has been proposed to visualize the temporal and spatial transformations of isopycnal displacements. It illustrates the oscillations of isopycnals over time, driven by cyclonic and anticyclonic eddies, and their effects on elevation and depression. The schematic highlights the horizontal spatial asymmetry between the faster, denser Denmark Strait Overflow Water (DSOW) and the slower ambient waters, showing how DSOW spans a greater horizontal range (Figure 13-b). Areas prone to instability, indicated by low Richardson numbers during isopycnal sloping, are also identified.

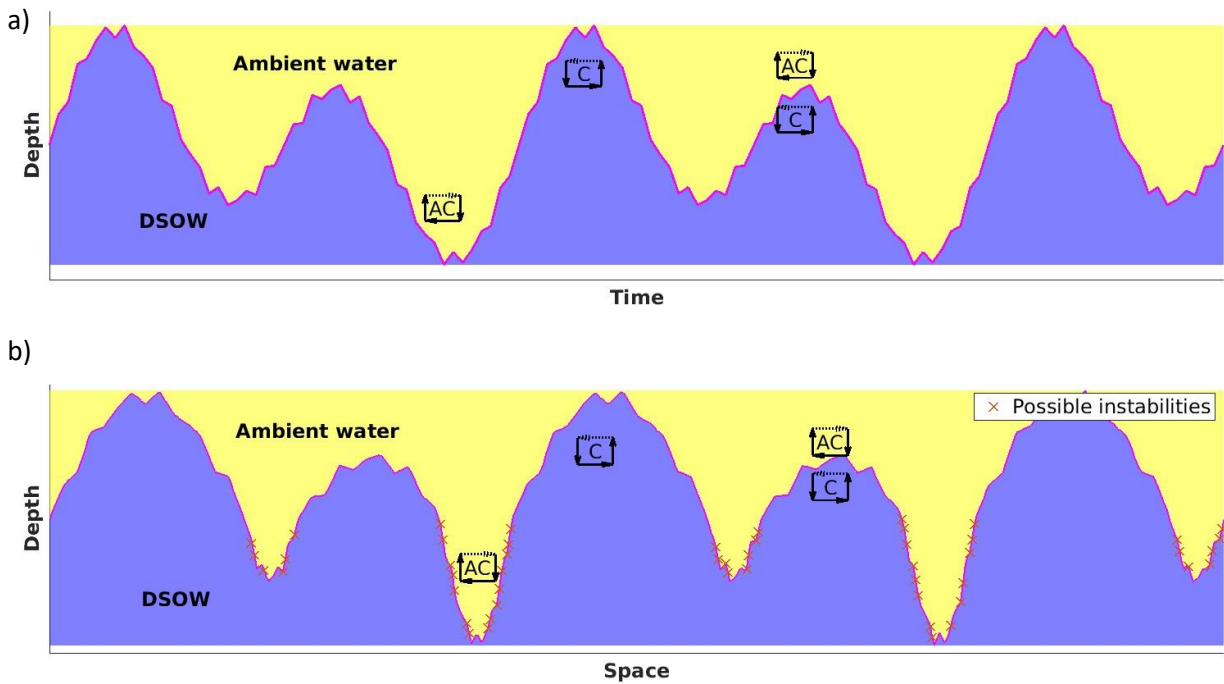


**Figure 13.** Scheme of isopycnal displacement in time (a) and transformation to space (b) with rotational patterns along the main isopycnal (AC = anticyclonic; C = cyclonic). The yellow area represents the slower and warmer ambient water whereas the blue area represents the colder and faster DSOW. The transformation into space results in a skewed isopycnal suggesting that the difference in velocity between the flow above and below the isopycnal have an influence on the spatial shape of the isopycnals.

## 6. Conclusions

The interface between the DSOW and ambient water was defined using the maximum vertical temperature gradient to build the reference interface layer ( $L_R$ ). The reference interface layer, positioned between 1°C and 4°C isotherms, was determined to have a mean depth of 1002.5 m with a standard deviation of  $\pm 67.4$  m. This confirms that the boundary between the two water masses is not fixed but exhibits vertical displacement of 10–100 meters. Above the reference layer, the ambient water exhibited mean temperature values of 4.1°C ( $\pm 0.96$ ) and salinity of 34.92 ( $\pm 0.04$ ) ‰, whereas below it the DSOW had a mean temperature of 1.2°C ( $\pm 0.98$ ) and salinity of 34.82 ( $\pm 0.03$ ) ‰.

The velocities of the two water masses show distinct differences in magnitude and direction. The DSOW exhibited a mean along-stream velocity ( $u_a$ ) of 0.75 m/s ( $\pm 0.20$  m/s), significantly higher than the 0.27 m/s ( $\pm 0.18$  m/s) of the ambient water. The cross-stream velocity ( $u_c$ ) for the DSOW was 0.07 m/s ( $\pm 0.14$  m/s), while the ambient water exhibited a negative mean  $u_c$  of -0.12 m/s ( $\pm 0.20$  m/s). The DSOW's mean flow direction was 152.1° ( $\pm 1.54^\circ$ ), while the ambient water had a mean direction of 172.9° ( $\pm 1.13^\circ$ ), indicating a westward shift in the ambient flow relative to the DSOW.

Spectral analysis revealed that the velocity and temperature signals were dominated by two main frequency peaks: one at 1.09 days<sup>-1</sup> (in the range of diurnal tides), contributing 17.47% to the velocity variance and 6.17% of the temperature variance, and a second low-frequency peak at 0.54 days<sup>-1</sup> (period = 1.8 days), which explained 48.33% of the velocity variance and 50.69% of the temperature variance. This low-frequency peak corresponds to mesoscale variability and indicates that mesoscale events, with periods of 1.8 days ( $\pm 0.2$  days), account for nearly 50% of the total variability in both velocity and temperature.

The horizontal scales of mesoscale events were estimated using the mean velocities of the DSOW and ambient water. For the DSOW, the along-stream displacement was ~116.64 km, and the cross-stream displacement was ~10.10 km, resulting in a total displacement magnitude of ~117.08 km. In contrast, the ambient water exhibited a much smaller along-stream displacement (~42.00 km) and a cross-stream displacement of ~-18.66 km, leading to a total displacement magnitude of ~45.96 km. This demonstrates that the cold water events (DSOW) have a much larger horizontal footprint compared to the warm water events, highlighting the horizontal spatial asymmetry in the size of the mesoscale features.

Wavelet analysis of the velocity components revealed a possible relationship between low-frequency mesoscale events and high-frequency fluctuations. Low-frequency events are particularly notable in the along-stream velocity component ( $u_a$ ). On the other hand, high-frequency variability appeared to be more pronounced in the cross-stream velocity component ( $u_c$ ), with distinct shifts associated with the transitions between cold and warm water events. This indicates that the low-frequency mesoscale events along-stream could modulate the high-frequency fluctuations cross-stream, particularly during the transition between warm and cold water events.

The analysis of velocity anomalies along the region of maximum temperature gradient points to the possibility of eddies or meanders moving along the interface. Cyclonic and anticyclonic patterns along the reference layer seem to alienate with the vertical displacements in isopycnal surfaces through processes such as upwelling or downwelling (respectively), which could explain the variability in depth of the isopycnals. Although this remains a qualitative inference, the rotation patterns coupled to changes in temperature signals supports the idea that these mesoscale eddies may be responsible for the displacement and fluctuations in isopycnals.

The Richardson number (Ri) analysis revealed that the water column was prone to vertical shear instabilities when Ri dropped below  $\frac{1}{4}$ , particularly below the reference interface layer. The Richardson number dropped below this threshold intermittently, indicating moments of instability and the potential for vertical mixing. These unstable conditions occurred predominantly in the DSOW layer, where the stratification ( $N^2$ ) was high, but the velocity shear (Sh) exceeded the stratification, creating conditions conducive to mixing. The occurrence of vertical shear instabilities was linked to periods when the vertical shear (Sh) displaced below the reference layer, suggesting that the most favorable conditions for instability are associated with the displacement of the maximum vertical shear beneath the main isopycnal  $27.8 \text{ kg/m}^3$ .

The occurrence of vertical shear instabilities below the reference layer suggests that vertical mixing processes may be more intense in the DSOW layer, potentially influencing the vertical exchange between the DSOW and the ambient water. This finding implies that the interaction between these two water masses is not only influenced by horizontal dynamics but also by vertical mixing processes, which could have significant implications for the distribution of heat, salt, and nutrients in this region.

## 7. References

Dickson, R. R., & Brown, J. (1994). The production of North Atlantic Deep Water: sources, rates, and pathways. *Journal of Geophysical Research: Oceans*, 99(C6), 12319-12341.

[DOI:10.1029/94JC00530](https://doi.org/10.1029/94JC00530)

Girton, J. B. (2001). Dynamics of transport and variability in the Denmark Strait overflow. University of Washington.

Girton, J. B., & Sanford, T. B. (2003). Descent and modification of the overflow plume in the Denmark Strait. *Journal of Physical Oceanography*, 33(7), 1351-1364. [DOI:10.1175/1520-0485\(2003\)033<1351:DAMOTO>2.0.CO;2](https://doi.org/10.1175/1520-0485(2003)033<1351:DAMOTO>2.0.CO;2)

Harden, B.E., Pickart, R.S., Valdimarsson, H., Våge, K., de Steur, L., Richards, C., Bahr, F., Torres, D., Børve, E., Jónsson, S. and Macrander, A., 2016. Upstream sources of the Denmark Strait Overflow: Observations from a high-resolution mooring array. Deep Sea Research Part I: Oceanographic Research Papers, 112, pp.94-112. [DOI:10.1016/j.dsr.2016.02.007](https://doi.org/10.1016/j.dsr.2016.02.007)

Koszalka, I. M., Haine, T. W. N., & Magaldi, M. G. (2017). Mesoscale mixing of the Denmark Strait Overflow in the Irminger Basin. *Ocean Modelling*, 112, 90–98.

<https://doi.org/10.1016/j.ocemod.2017.02.007>

Kanzow, T., von Albedyll, L., Benz, F., Elmer, C., Kritsotakis, S., Lauber, J., Ali, S. M., Muchow, M., Münchow, A., Trace-Kleeberg, S., Werner, E., Wett, S., & Zippel, A. (2018). *MARIA S. MERIAN-Berichte: Nordic Seas Exchanges, Cruise No. MSM 76, August 11 – September 11, 2018*. Alfred-Wegener-Institut Helmholtz-Zentrum für Polar- und Meeresforschung.

Lilly, J. M. (2024). *Ocean/Atmosphere Time Series Analysis*. Planetary Science Institute. Updated July 28, 2024. Retrieved from:

[https://www.jmlilly.net/course/labs/html/WaveletAnalysis\\_Matlab.html](https://www.jmlilly.net/course/labs/html/WaveletAnalysis_Matlab.html)

Macrander, A., Käse, R. H., Send, U., Valdimarsson, H., & Jónsson, S. (2007). Spatial and temporal structure of the Denmark Strait Overflow revealed by acoustic observations. *Ocean Dynamics*, 57, 75-89. [DOI:10.1007/s10236-007-0101-x](https://doi.org/10.1007/s10236-007-0101-x)

Moritz, M., Jochumsen, K., North, R. P., Quadfasel, D., & Valdimarsson, H. (2019). Mesoscale eddies observed at the Denmark Strait sill. *Journal of Geophysical Research: Oceans*, 124(11), 7947-7961. [DOI:10.1029/2019JC015189](https://doi.org/10.1029/2019JC015189)

Olbers, D., Willebrand, J., & Eden, C. (2012). *Ocean Dynamics*. Springer Science & Business Media, 703 pages. [DOI: 10.1007/978-3-642-23450-7](https://doi.org/10.1007/978-3-642-23450-7)

Thomson, D. J. (1982). "Spectrum estimation and harmonic analysis." Proceedings of the IEEE, 70(9), 1055–1096. [DOI:10.1109/PROC.1982.12433](https://doi.org/10.1109/PROC.1982.12433)

Voet, G., & Quadfasel, D. (2010). Entrainment in the Denmark Strait overflow plume by meso-scale eddies. *Ocean Science*, 6(1), 301-310. [DOI:10.5194/os-6-301-2010](https://doi.org/10.5194/os-6-301-2010)

Von Appen, W. J., Mastropole, D., Pickart, R. S., Valdimarsson, H., Jónsson, S., & Girton, J. B. (2017). On the nature of the mesoscale variability in Denmark Strait. *Journal of Physical Oceanography*, 47(3), 567-582. [DOI:10.1175/JPO-D-16-0127.1](https://doi.org/10.1175/JPO-D-16-0127.1)

Von Appen, W.-J. (2019). *Raw data including physical oceanography from mooring DS-C-18 recovered during Maria S. Merian cruise MSM76*. PANGAEA.

<https://doi.org/10.1594/PANGAEA.904526>

Von Appen, Wilken-Jon, Inga M. Koszalka, Robert S. Pickart, Thomas WN Haine, Dana Mastropole, Marcello G. Magaldi, Héðinn Valdimarsson, James Girton, Kerstin Jochumsen, and Gerd Krahmann (2014). "The East Greenland Spill Jet as an important component of the Atlantic meridional overturning circulation." *Deep Sea Research Part I: Oceanographic Research Papers* 92: 75-84. [DOI:10.1016/j.dsr.2014.06.002](https://doi.org/10.1016/j.dsr.2014.06.002)

## Supplementary figures

### Supplementary figures to figures 11 and 12.

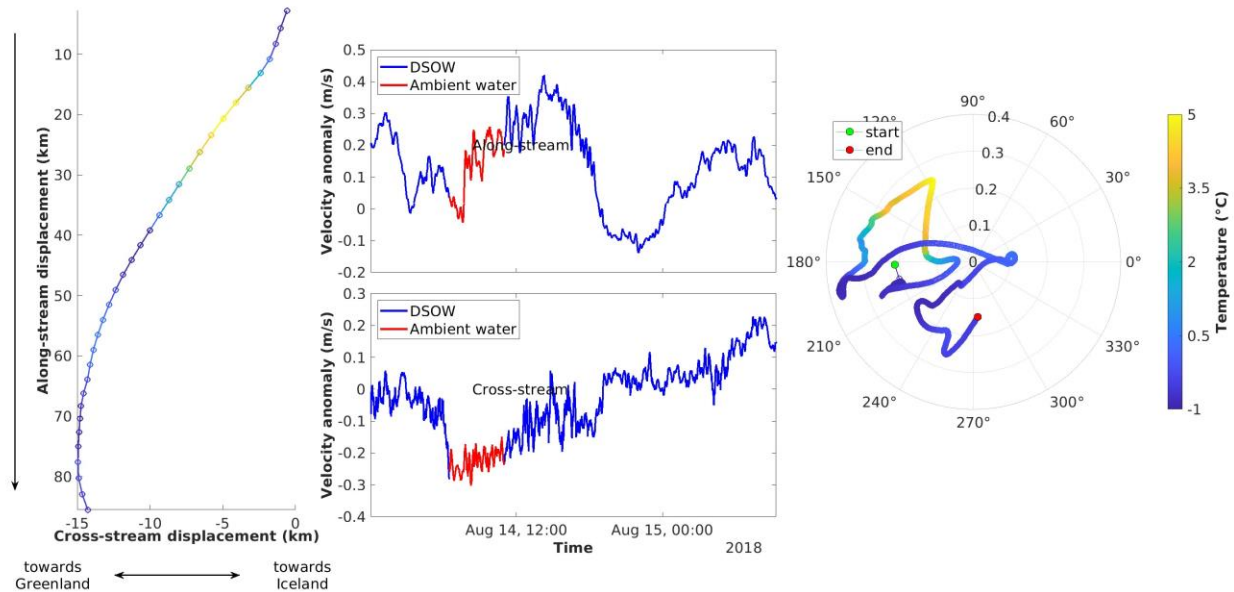


**Figure 11.1.** Characterization of cold mesoscale fluctuation (not clear) on August 14th-15th. (a) Figure 7-b zoomed in at the time of a cold water fluctuation; (b & c) rotated velocity anomaly of  $u_a$  and  $u_c$ , respectively. (c) Polar hodograph of non-rotated velocity anomalies with temperature color.

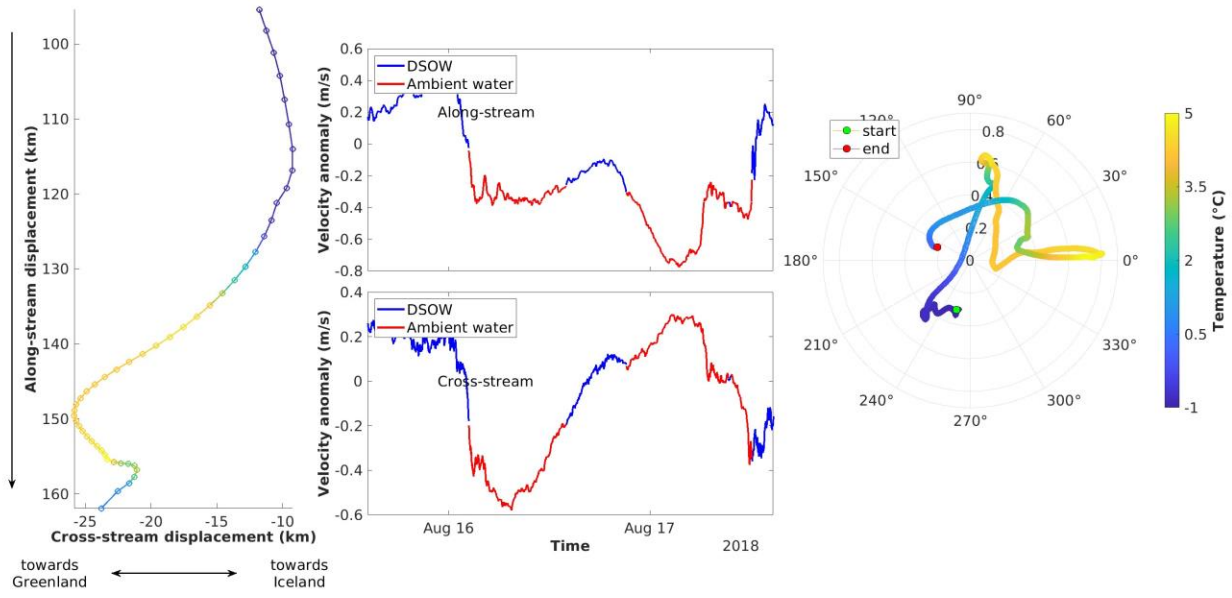


**Figure 12.1.** Characterization of warm mesoscale fluctuation (anticyclonic) on August 16th-17th. (a) Figure 7-b zoomed in at the time of a warm water fluctuation; (b & c) rotated velocity anomaly of  $u_a$  and  $u_c$ , respectively. (c) Polar hodograph of non-rotated velocity anomalies with temperature color.

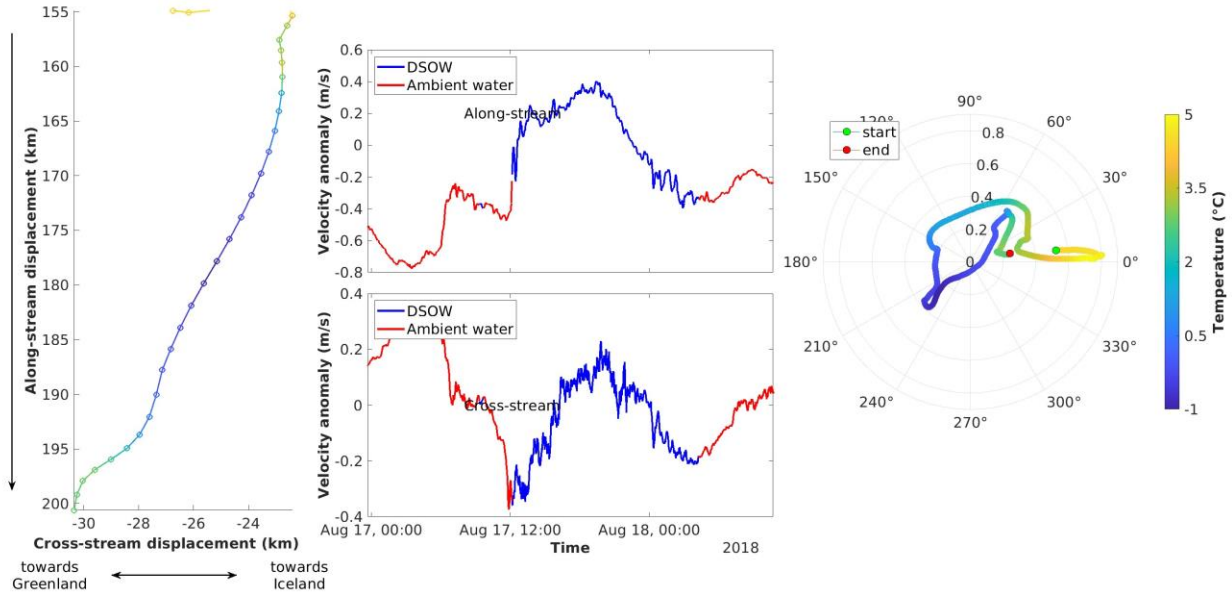


**Figure 11.2.** Characterization of cold mesoscale fluctuation (cyclonic) on August 17th-18th. (a) Figure 7-b zoomed

in at the time of a cold water fluctuation; (b & c) rotated velocity anomaly of  $u_a$  and  $u_c$ , respectively. (c) Polar hodograph of non-rotated velocity anomalies with temperature color.

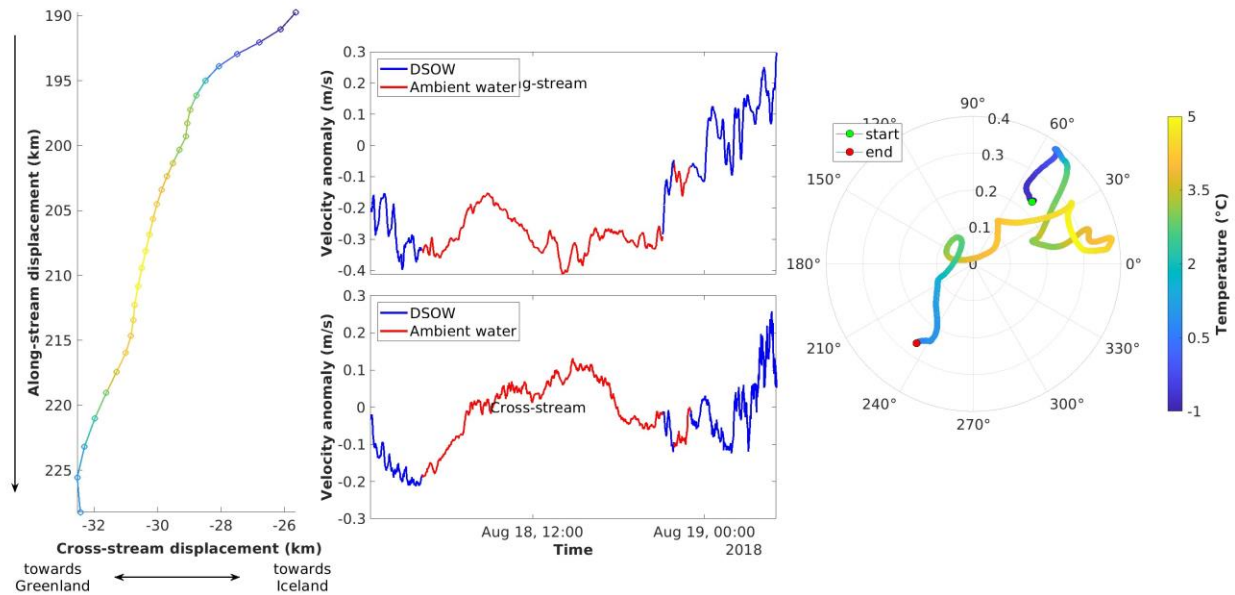


**Figure 12.2.** Characterization of warm mesoscale fluctuation (not clear) on August 18th-19th. (a) Figure 7-b zoomed in at the time of a warm water fluctuation; (b & c) rotated velocity anomaly of  $u_a$  and  $u_c$ , respectively. (c) Polar hodograph of non-rotated velocity anomalies with temperature color.

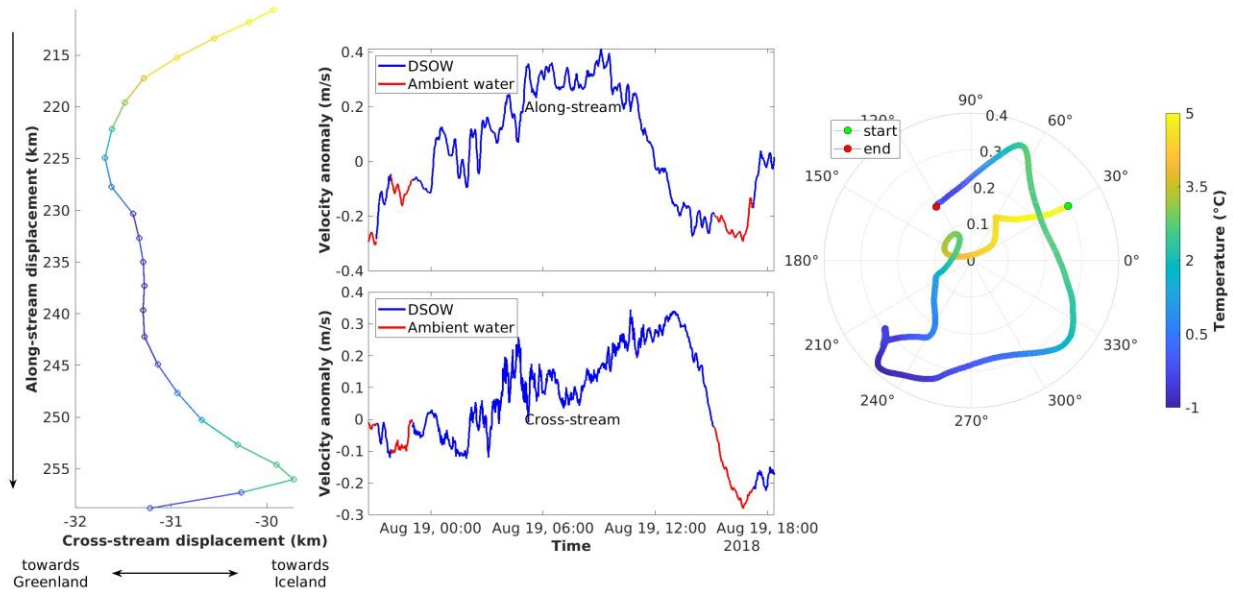


**Figure 11.3.** Characterization of cold mesoscale fluctuation (cyclonic) on August 19th. (a) Figure 7-b zoomed in at the time of a cold water fluctuation; (b & c) rotated velocity anomaly of  $u_a$  and  $u_c$ , respectively. (c) Polar hodograph of non-rotated velocity anomalies with temperature color.

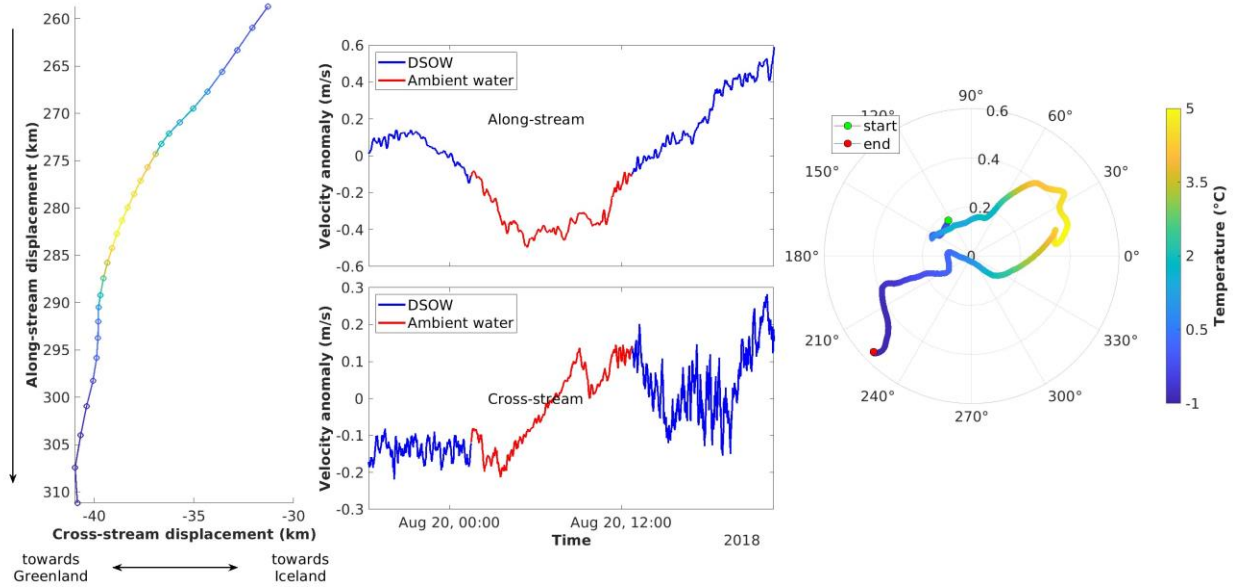


**Figure 12.3.** Characterization of warm mesoscale fluctuation (anticyclonic) on August 20th. (a) Figure 7-b zoomed in at the time of a warm water fluctuation; (b & c) rotated velocity anomaly of  $u_a$  and  $u_c$ , respectively. (c) Polar hodograph of non-rotated velocity anomalies with temperature color.

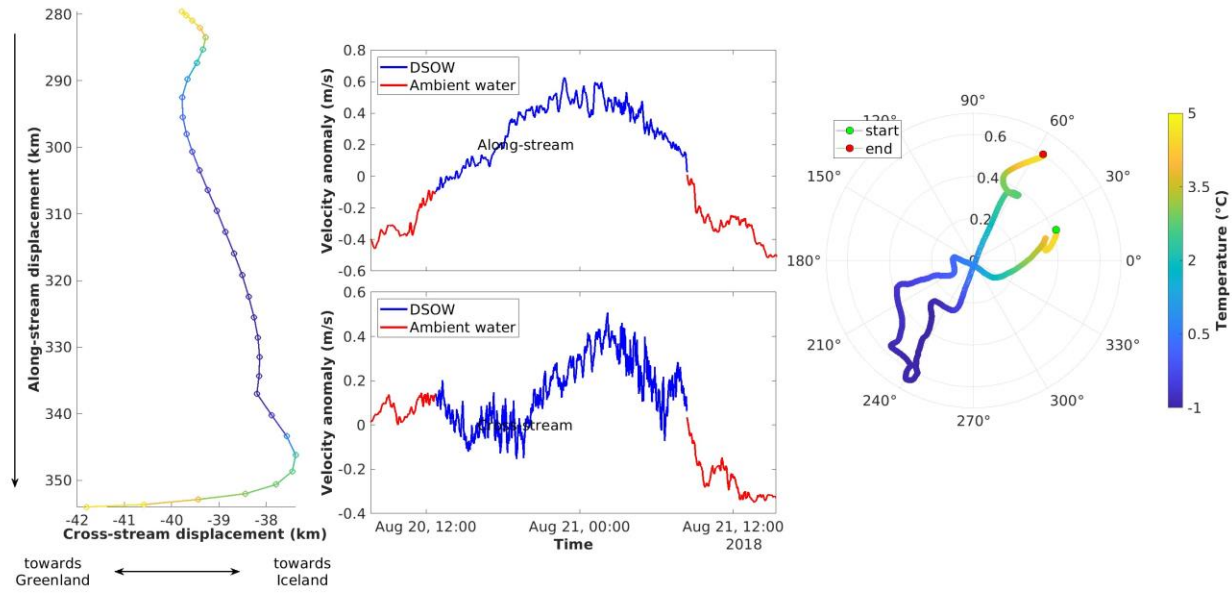


**Figure 11.4.** Characterization of cold mesoscale fluctuation (cyclonic) on August 20th-21st. (a) Figure 7-b zoomed in at the time of a cold water fluctuation; (b & c) rotated velocity anomaly of  $u_a$  and  $u_c$ , respectively. (c) Polar hodograph of non-rotated velocity anomalies with temperature color.

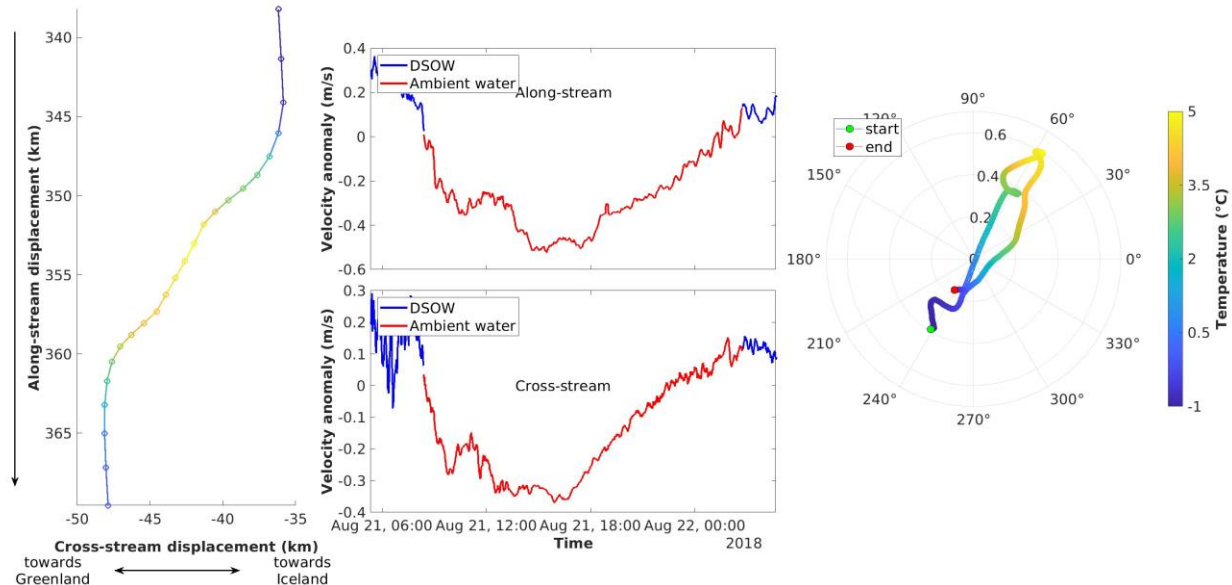


**Figure 12.4.** Characterization of warm mesoscale fluctuation (anticyclonic) on August 21st-22nd. (a) Figure 7-b zoomed in at the time of a warm water fluctuation; (b & c) rotated velocity anomaly of  $u_a$  and  $u_c$ , respectively. (c) Polar hodograph of non-rotated velocity anomalies with temperature color.

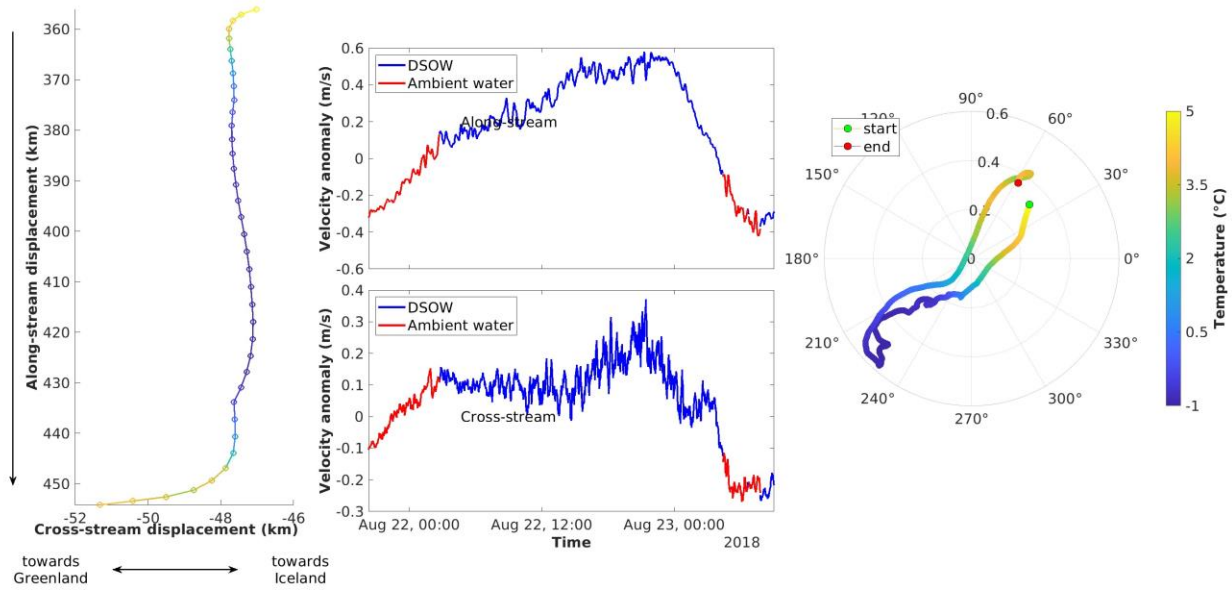


**Figure 11.5.** Characterization of cold mesoscale fluctuation (not clear) on August 22nd-23rd. (a) Figure 7-b zoomed in at the time of a cold water fluctuation; (b & c) rotated velocity anomaly of  $u_a$  and  $u_c$ , respectively. (c) Polar hodograph of non-rotated velocity anomalies with temperature color.

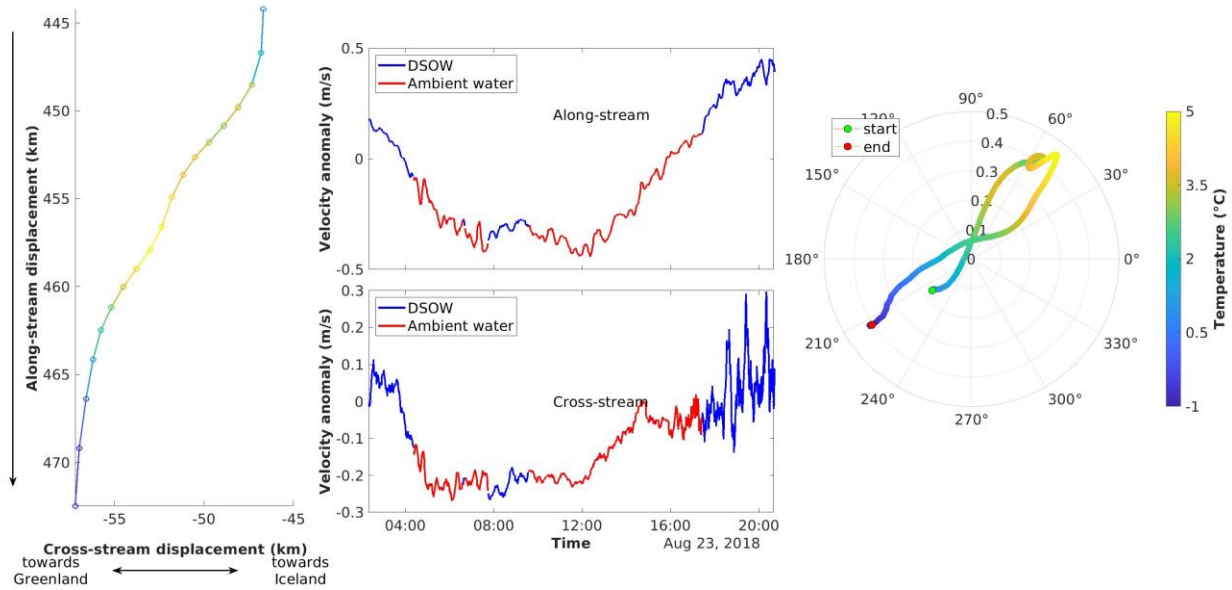


**Figure 12.5.** Characterization of warm mesoscale fluctuation (anticyclonic) on August 23rd. (a) Figure 7-b zoomed in at the time of a warm water fluctuation; (b & c) rotated velocity anomaly of  $u_a$  and  $u_c$ , respectively. (c) Polar hodograph of non-rotated velocity anomalies with temperature color.

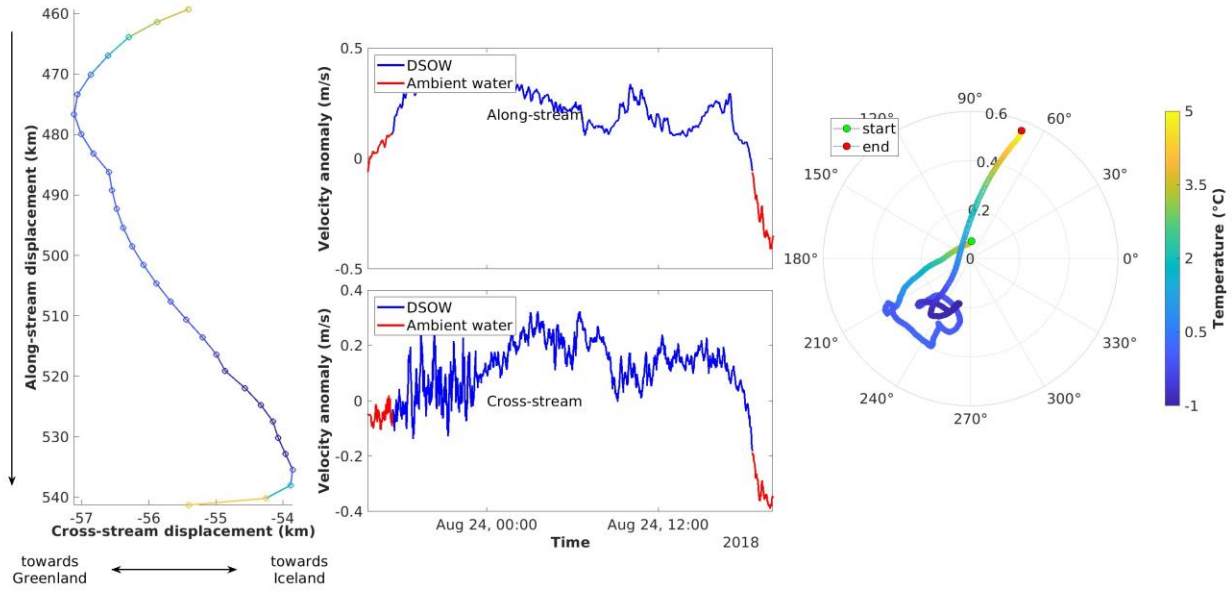


**Figure 11.6.** Characterization of cold mesoscale fluctuation (cyclonic) on August 24th. (a) Figure 7-b zoomed in at the time of a cold water fluctuation; (b & c) rotated velocity anomaly of  $u_a$  and  $u_c$ , respectively. (c) Polar hodograph of non-rotated velocity anomalies with temperature color.

## Supplementary figures for uppermost velocimeter

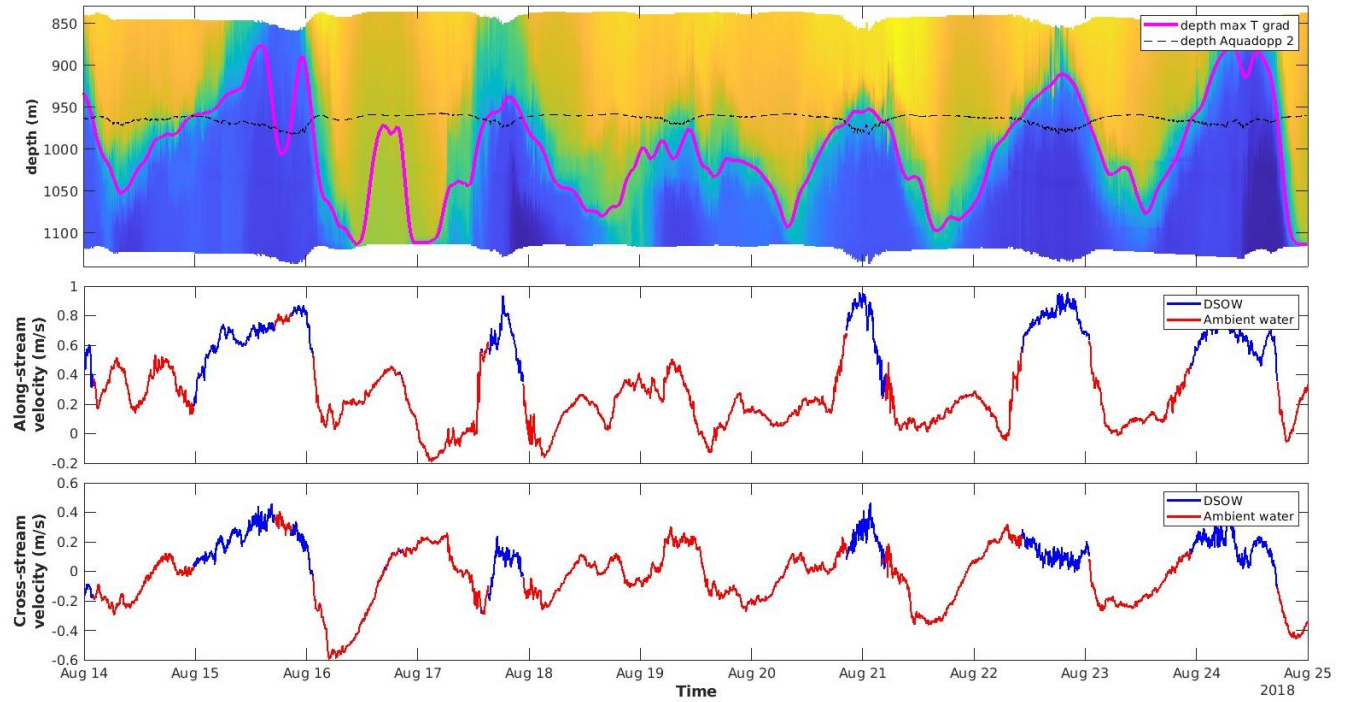


**Figure 14.** Division of DSOW and ambient water. (a) Water temperature and estimated pycnocline  $27.8 \text{ kg/m}^3$  (magenta line) using the maximum vertical temperature gradient ( $L_R$ ). The dashed black line represents the depth of the uppermost velocimeter. (b & c) Rotated horizontal velocity components ( $u_a$  &  $u_c$  respectively) at the uppermost velocimeter (mean depth = 970m) divided by waters above the  $L_R$  (red) and waters below the  $L_R$  (blue).

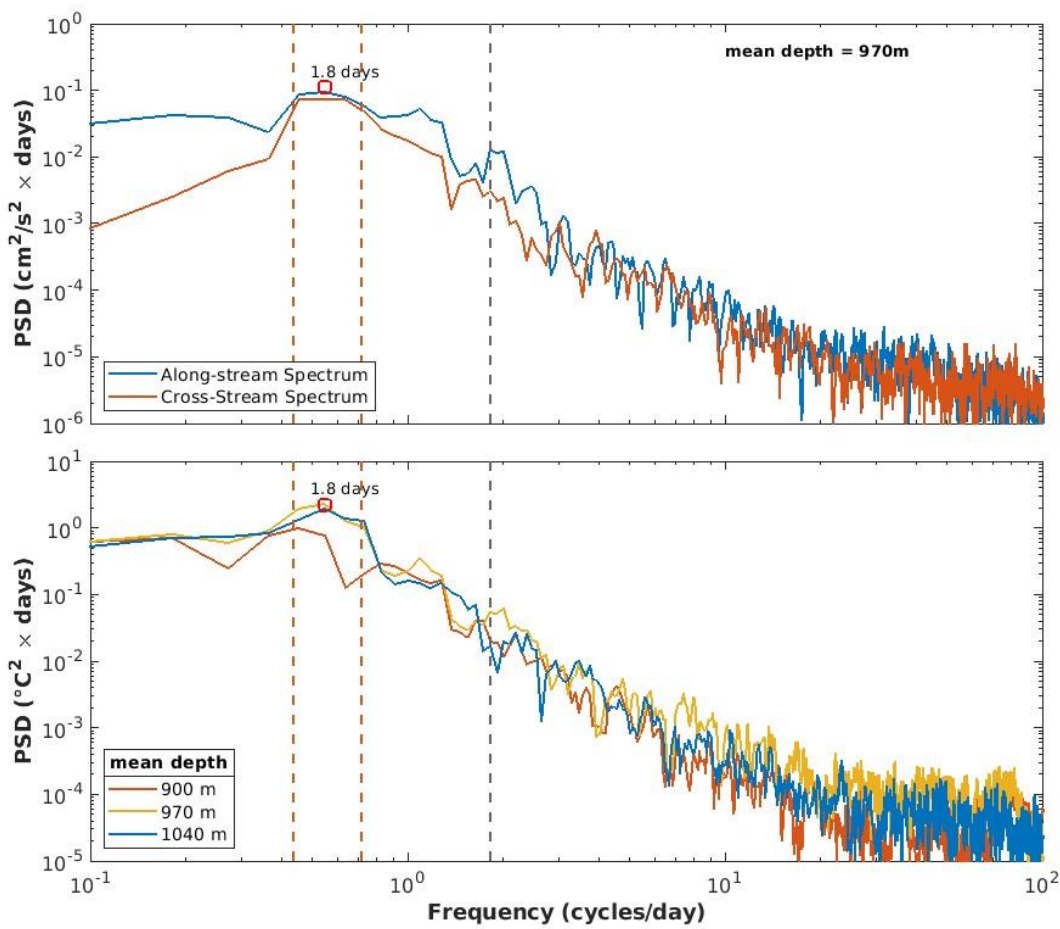


**Figure 15.** Power spectral density estimations of (a) rotated horizontal velocity components from uppermost velocimeter (mean depth = 970m); and (b) temperature data above (red), center (yellow) and below (blue) the region of maximum variability. The dotted grey line represents the Coriolis frequency (finertial = 1.82 days<sup>-1</sup>); and the two dashed black lines denote the interval of impact of the mesoscale variability [0.44, 0.74] days<sup>-1</sup> around the 0.54 days<sup>-1</sup> peak ( $T = 1.8$  days).

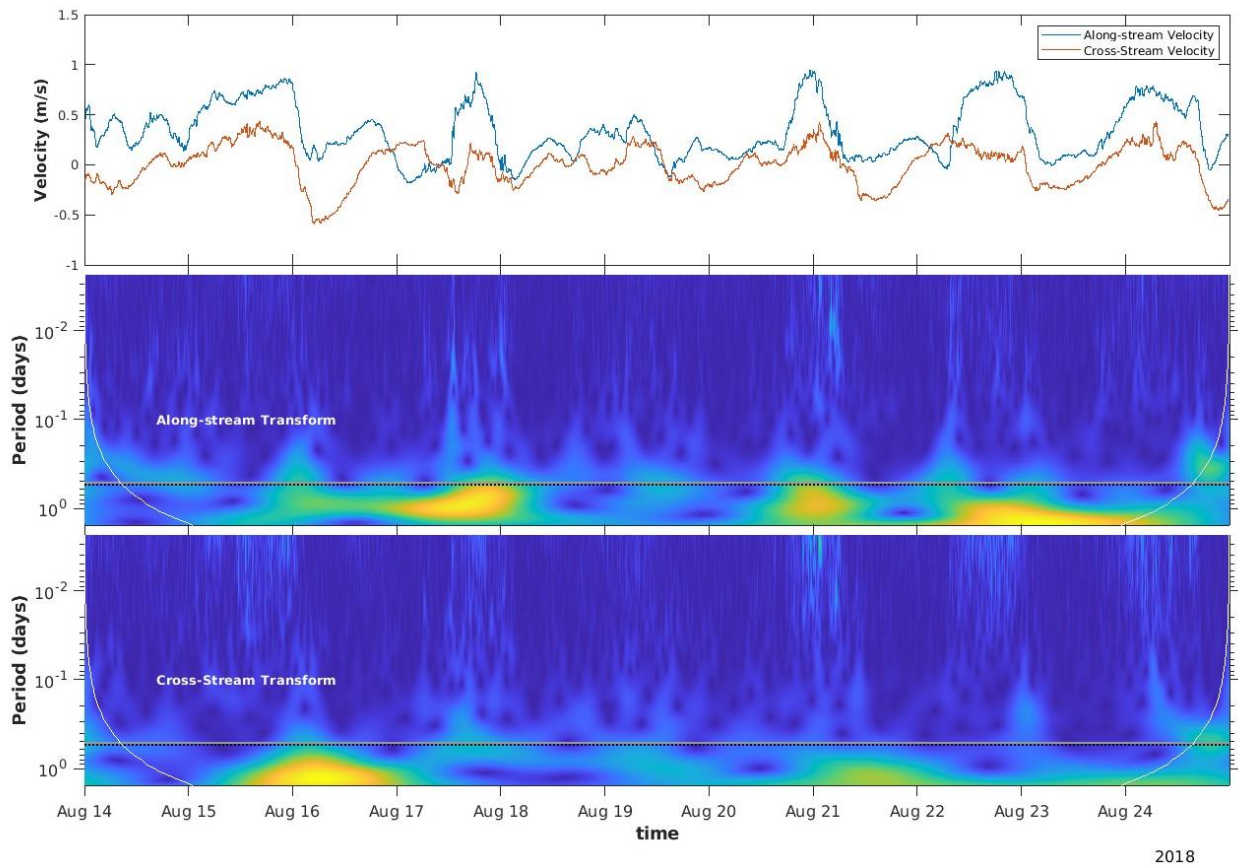


**Figure 16.** Wavelets analysis of velocities (mean depth = 970m). (a) Velocity components over time. (b) Along-stream wavelet transformation. (c) Cross-stream velocity transformation.

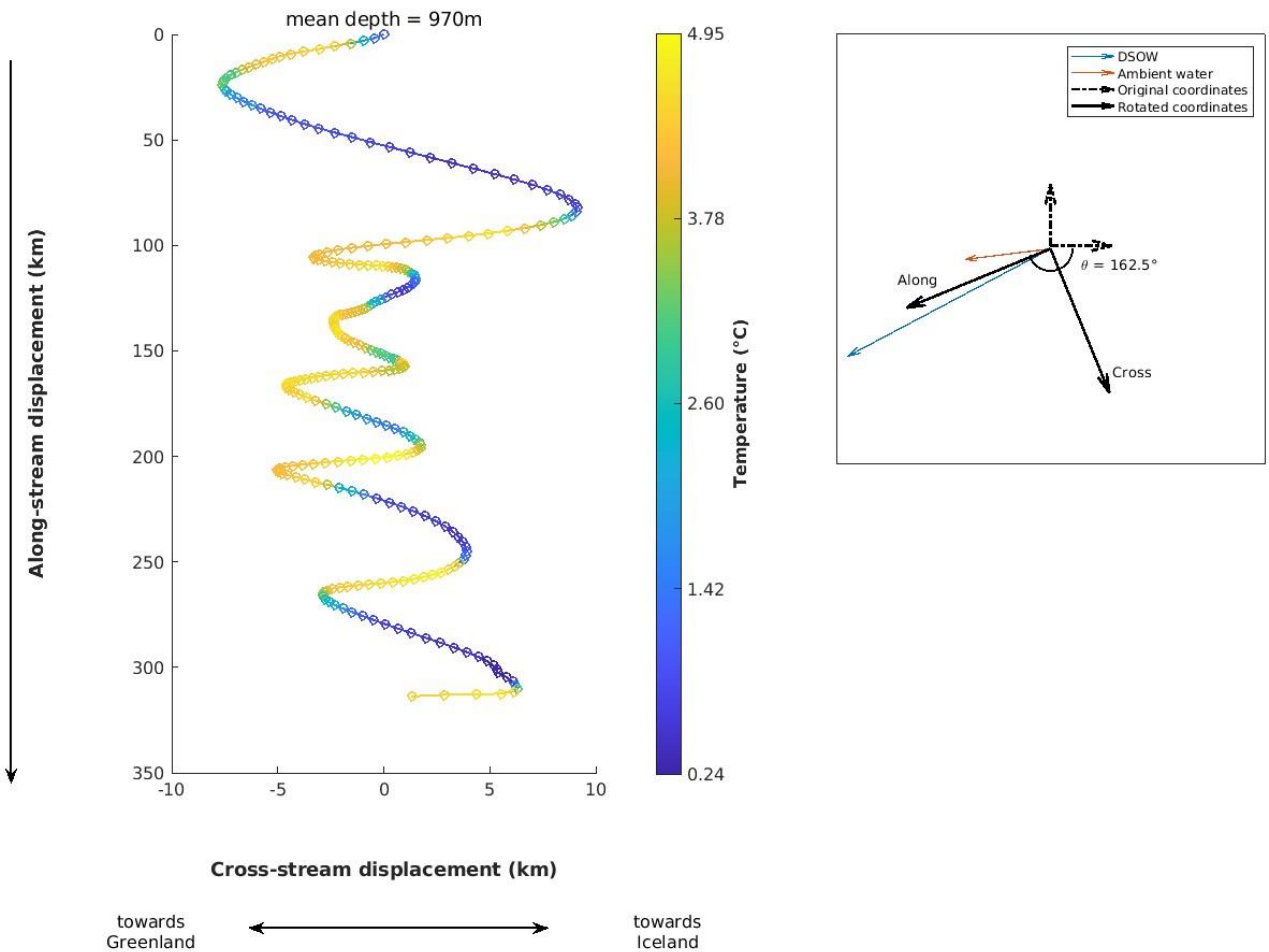


**Figure 17.** (a) Cumulative vector displacement diagram derived from the rotated velocity data from the uppermost velocimeter (mean depth = 970m) colored with its respective temperatures. (b) Scheme of coordinates rotation. The blue and red lines represent the mean direction and magnitude of the DSOW and the ambient water, respectively.

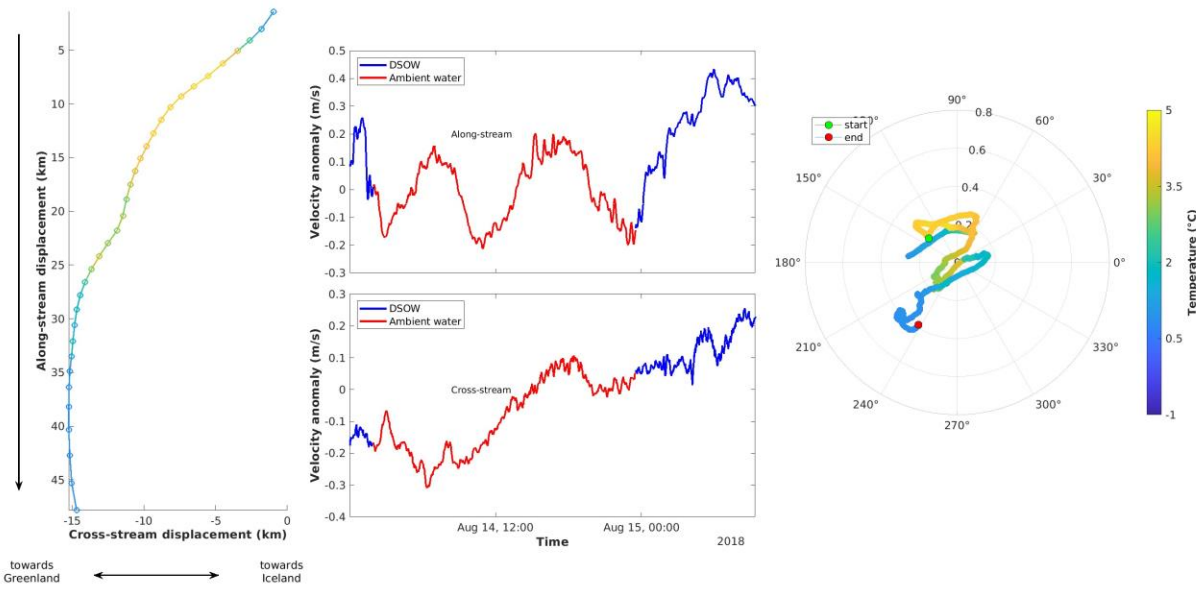


**Figure 18.** Figure 11.1 for the uppermost velocimeter.

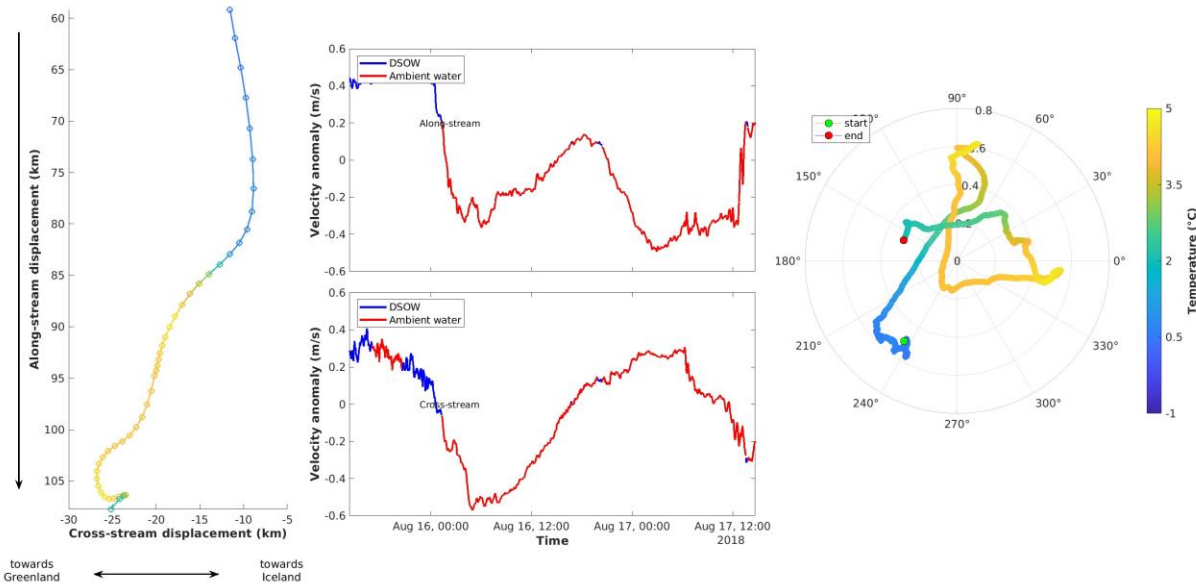


**Figure 19.** Figure 12.1 for the uppermost velocimeter.

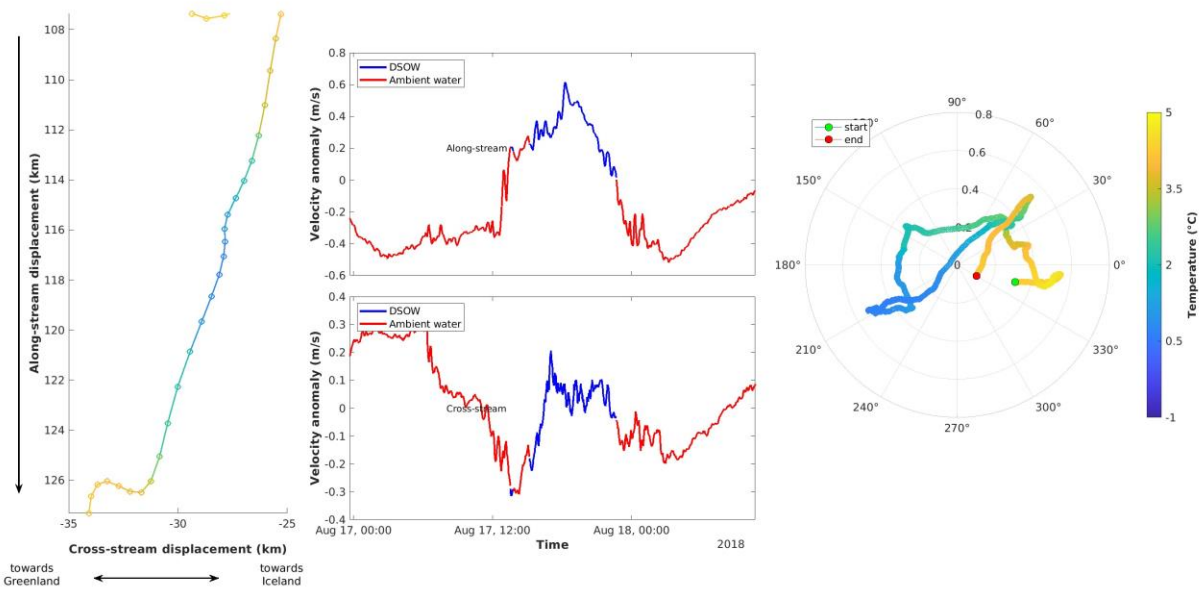


**Figure 20.** Figure 11.2 for the uppermost velocimeter.

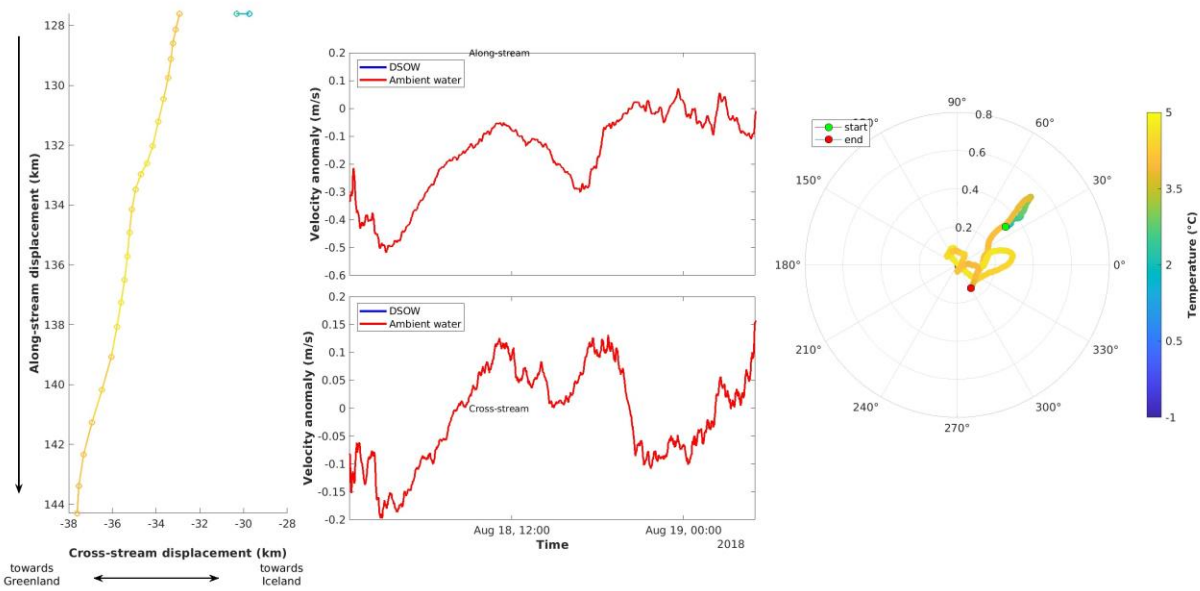


**Figure 21.** Figure 12.2 for the uppermost velocimeter.

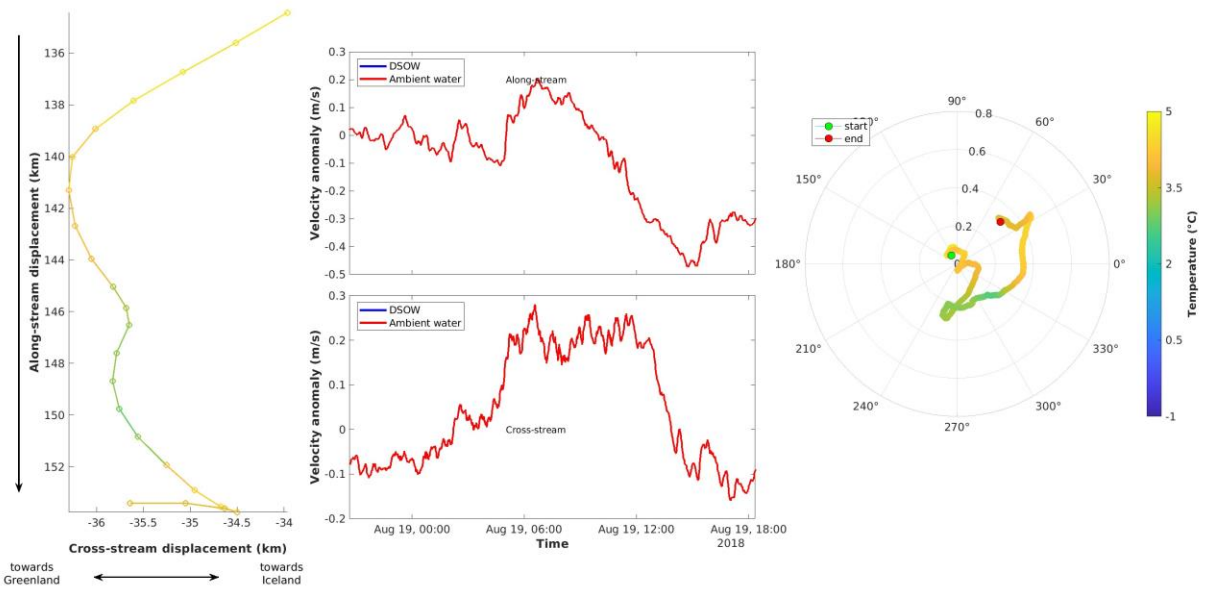


**Figure 22.** Figure 11.3 for the uppermost velocimeter.

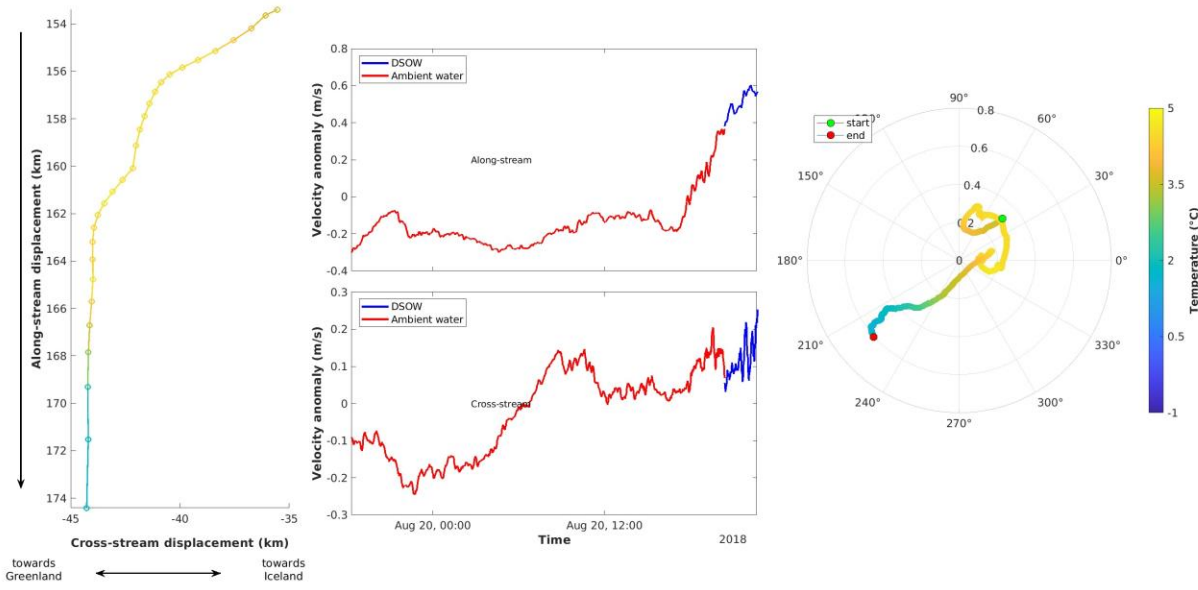


**Figure 23.** Figure 12.3 for the uppermost velocimeter.

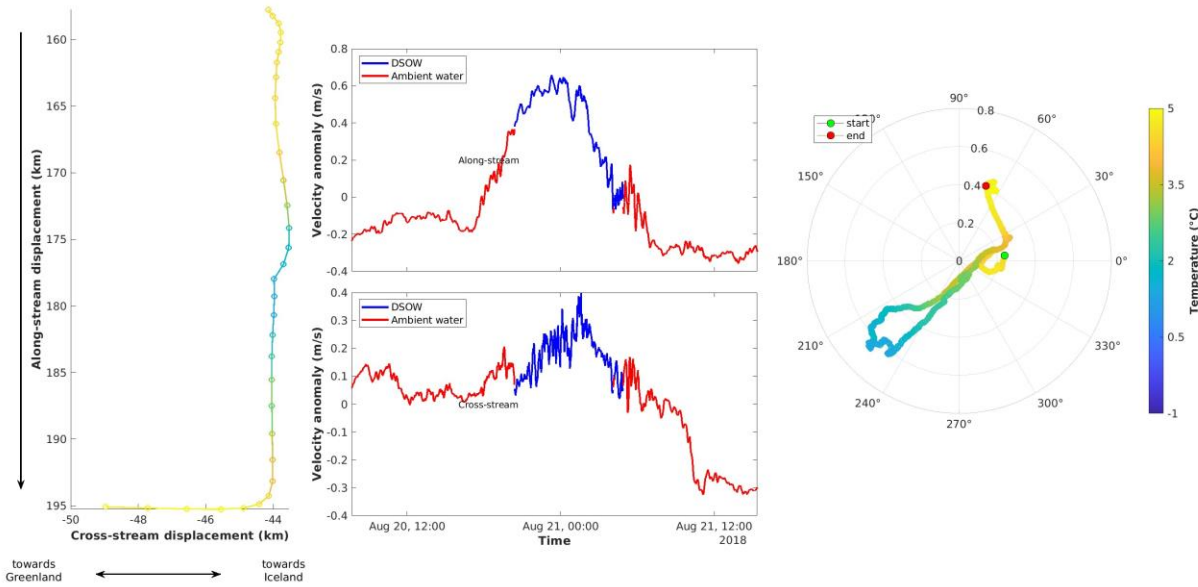


**Figure 24.** Figure 11.4 for the uppermost velocimeter.

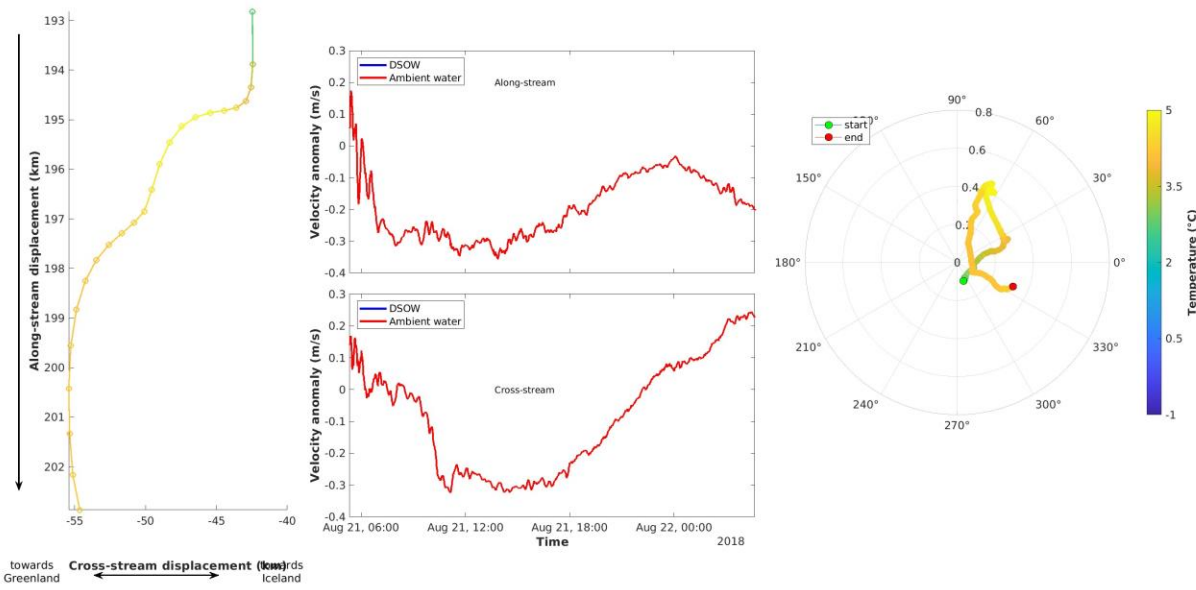


**Figure 25.** Figure 12.4 for the uppermost velocimeter.

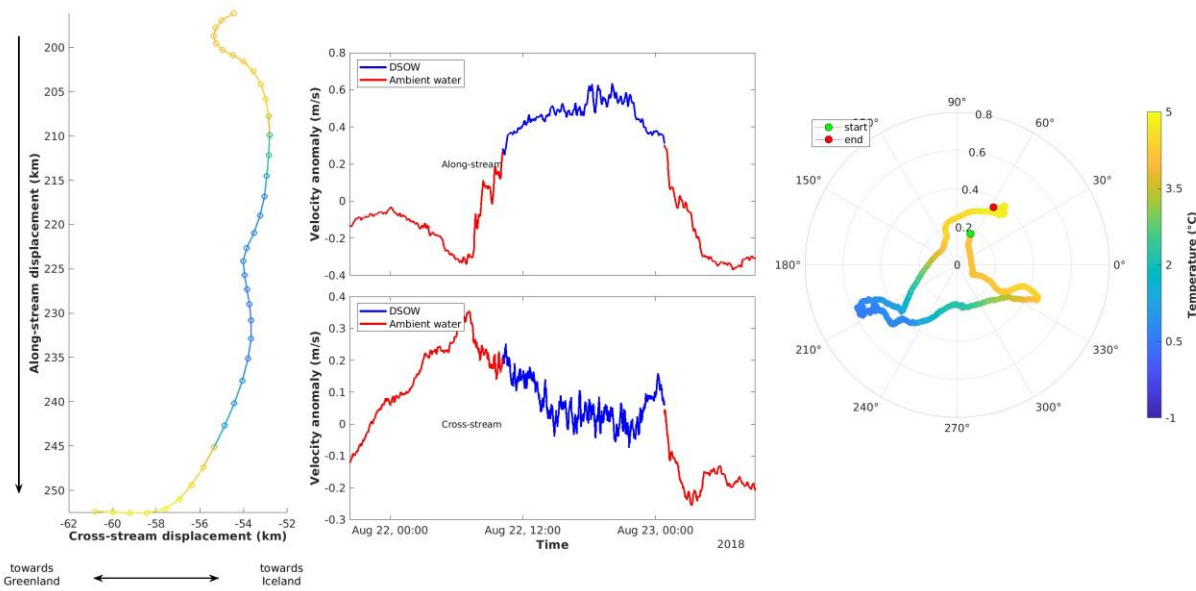


**Figure 26.** Figure 11.5 for the uppermost velocimeter.

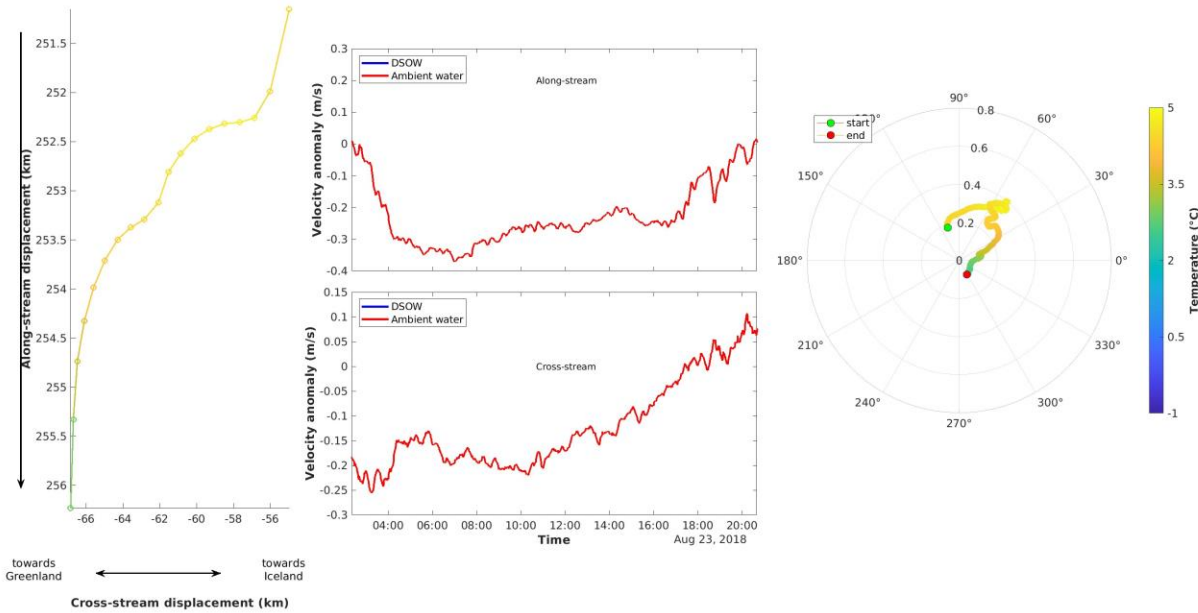


**Figure 27.** Figure 21.5 for the uppermost velocimeter.

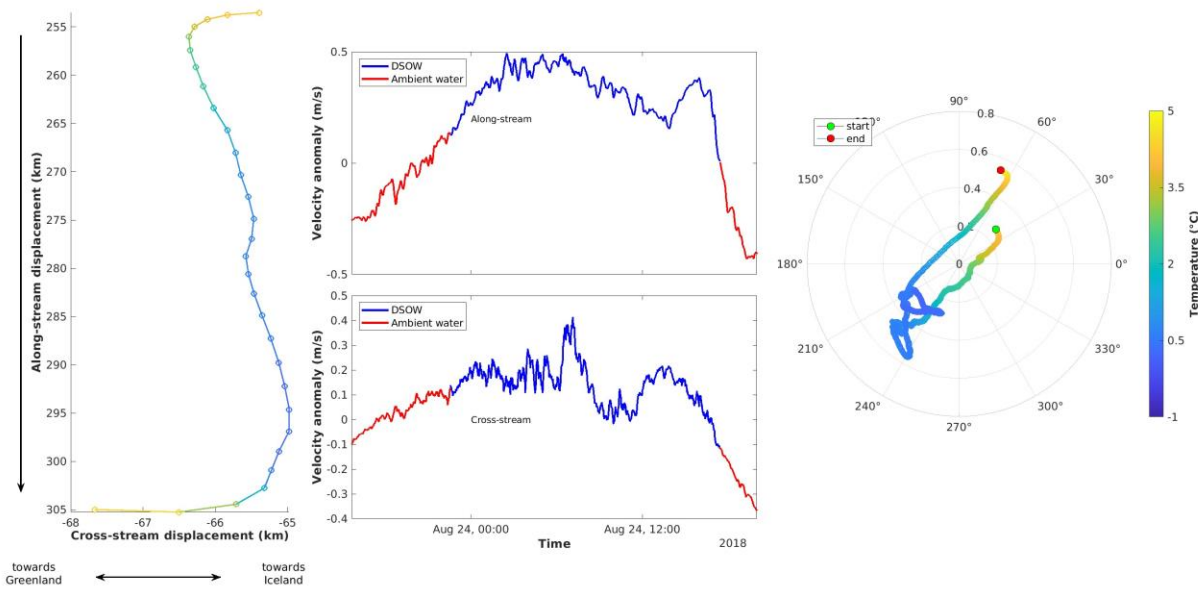


**Figure 28.** Figure 11.6 for the uppermost velocimeter.

## Supplementary figures for bottom velocimeter

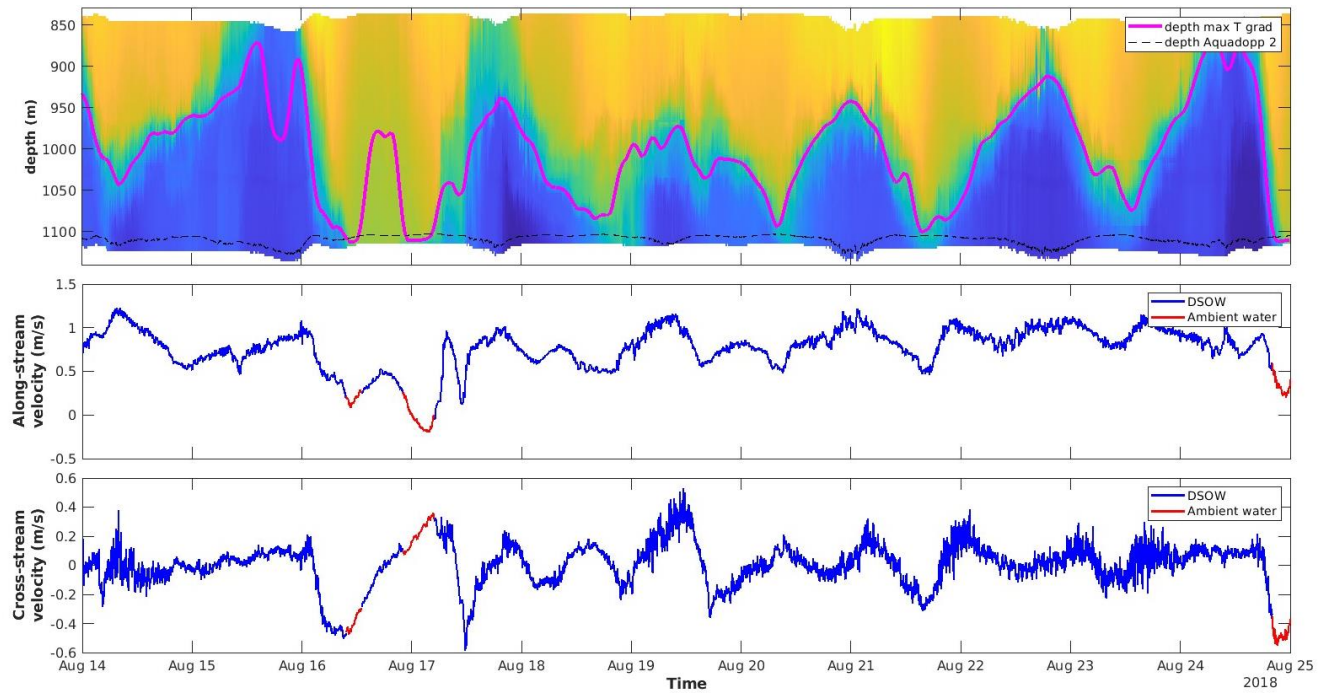


**Figure 29.** Division of DSOW and ambient water. (a) Water temperature and estimated pycnocline  $27.8 \text{ kg/m}^3$  (magenta line) using the maximum vertical temperature gradient ( $L_R$ ). The dashed black line represents the depth of the bottom velocimeter. (b & c) Rotated horizontal velocity components ( $u_a$  &  $u_c$  respectively) at the middle velocimeter (mean depth = 1120m) divided by waters above the  $L_R$  (red) and waters below the  $L_R$  (blue).

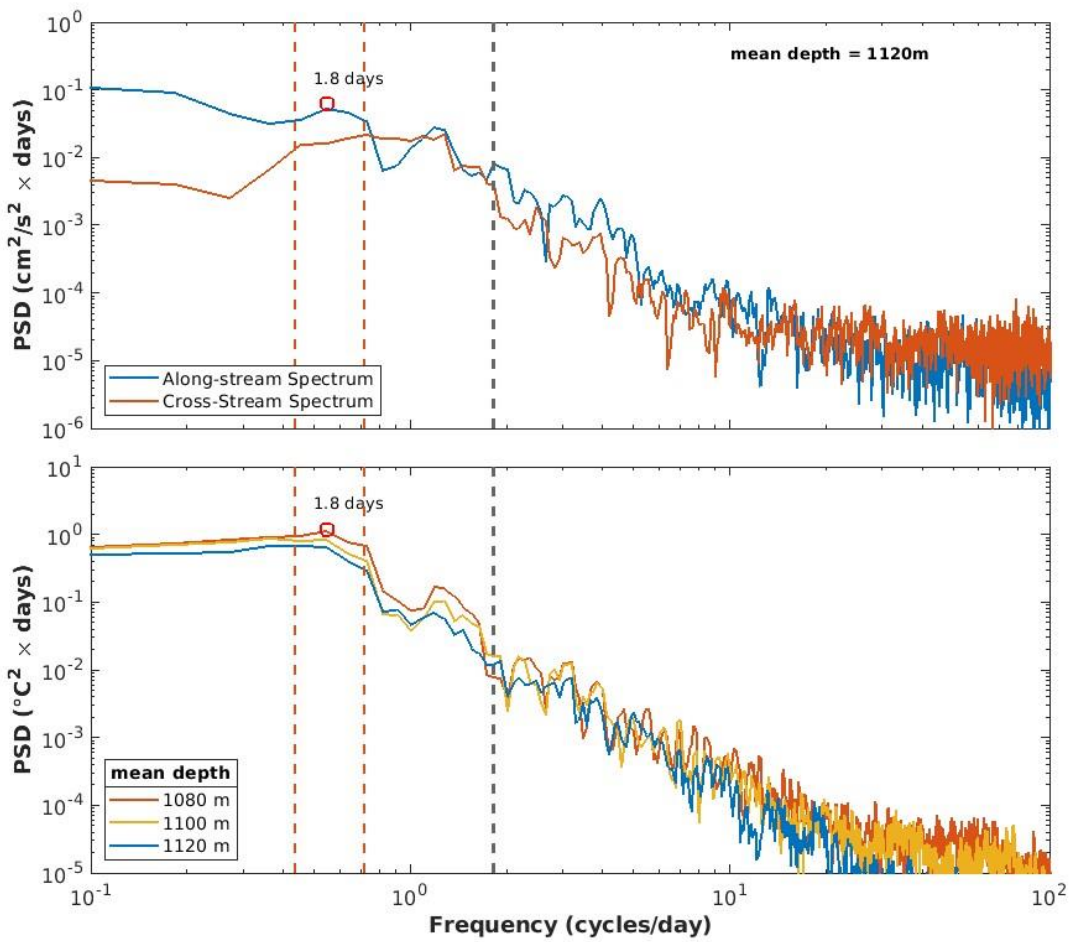


**Figure 30.** Power spectral density estimations of (a) rotated horizontal velocity components from bottom velocimeter (mean depth = 1120 m); and (b) temperature data above (red), center (yellow) and below (blue) the region of maximum variability. The dotted grey line represents the Coriolis frequency ( $f_{\text{inertial}} = 1.82 \text{ days}^{-1}$ ); and the two dashed black lines denote the interval of impact of the mesoscale variability [0.44, 0.74] days $^{-1}$  around the 0.54 days $^{-1}$  peak ( $T = 1.8$  days).

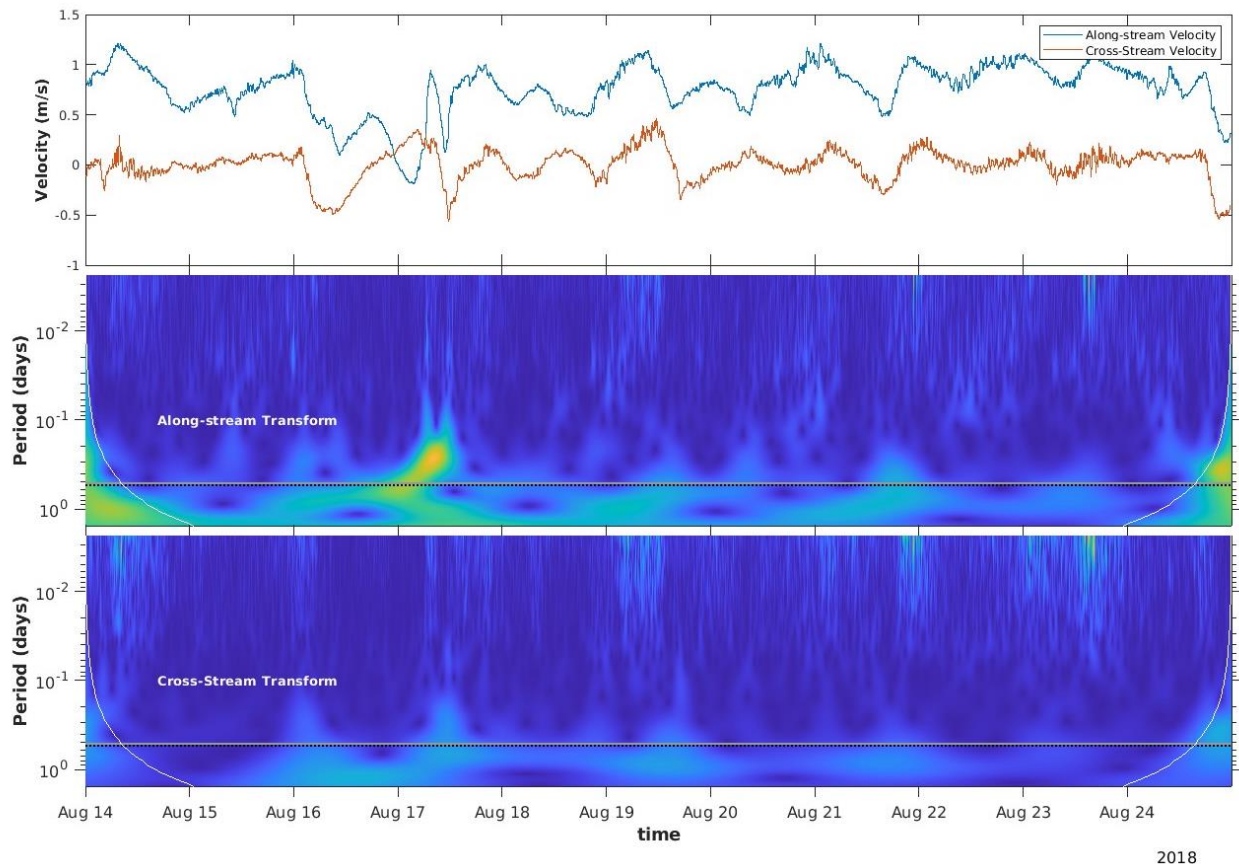


**Figure 31.** Wavelets analysis of velocities (mean depth = 1120m). (a) Velocity components over time. (b) Along-stream wavelet transformation. (c) Cross-stream velocity transformation.

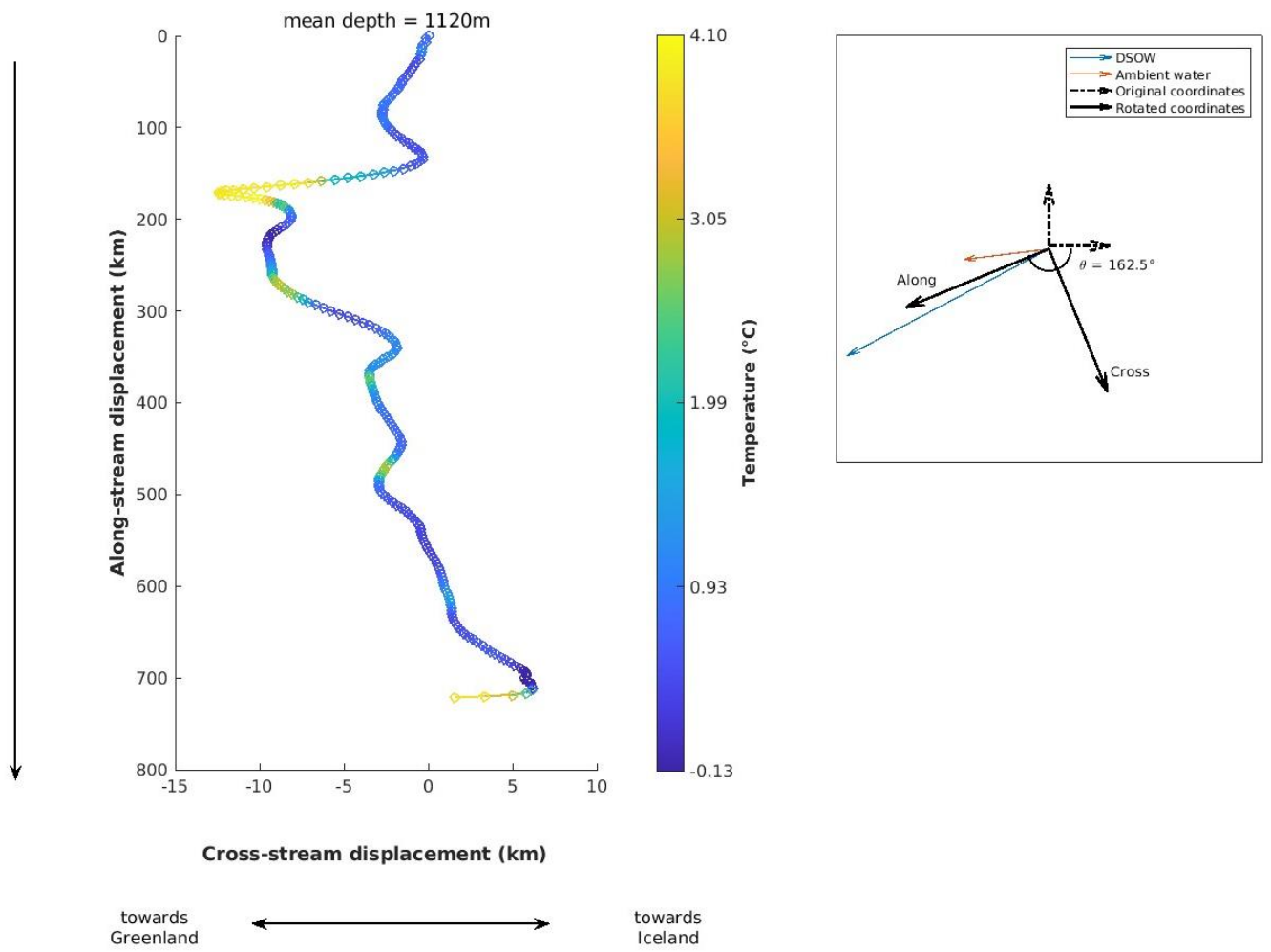


**Figure 32.** (a) Cumulative vector displacement diagram derived from the rotated velocity data from the bottom velocimeter (mean depth = 1120m) colored with its respective temperatures. (b) Scheme of coordinates rotation. The blue and red lines represent the mean direction and magnitude of the DSOW and the ambient water, respectively.

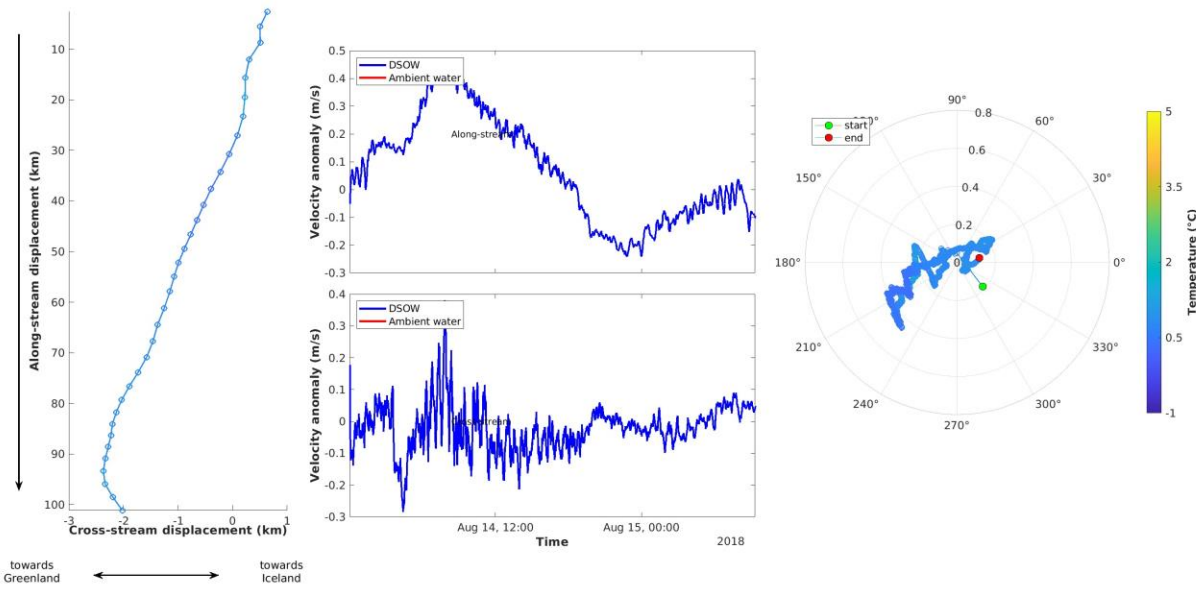


**Figure 33.** Figure 11.1 for the bottom velocimeter.

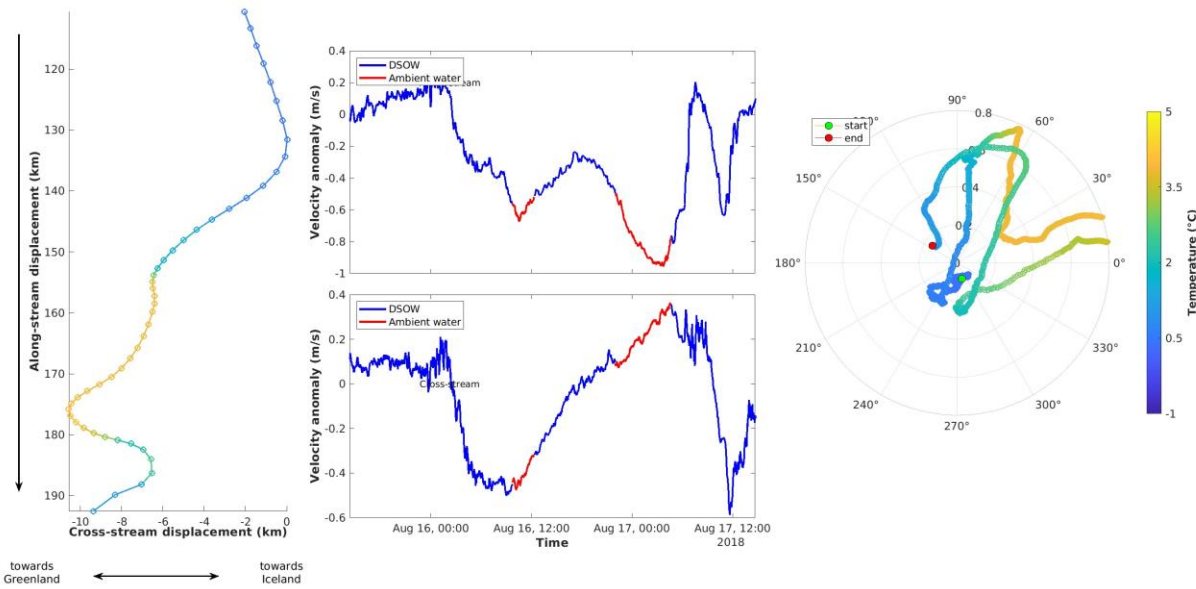


**Figure 34.** Figure 12.1 for the bottom velocimeter.

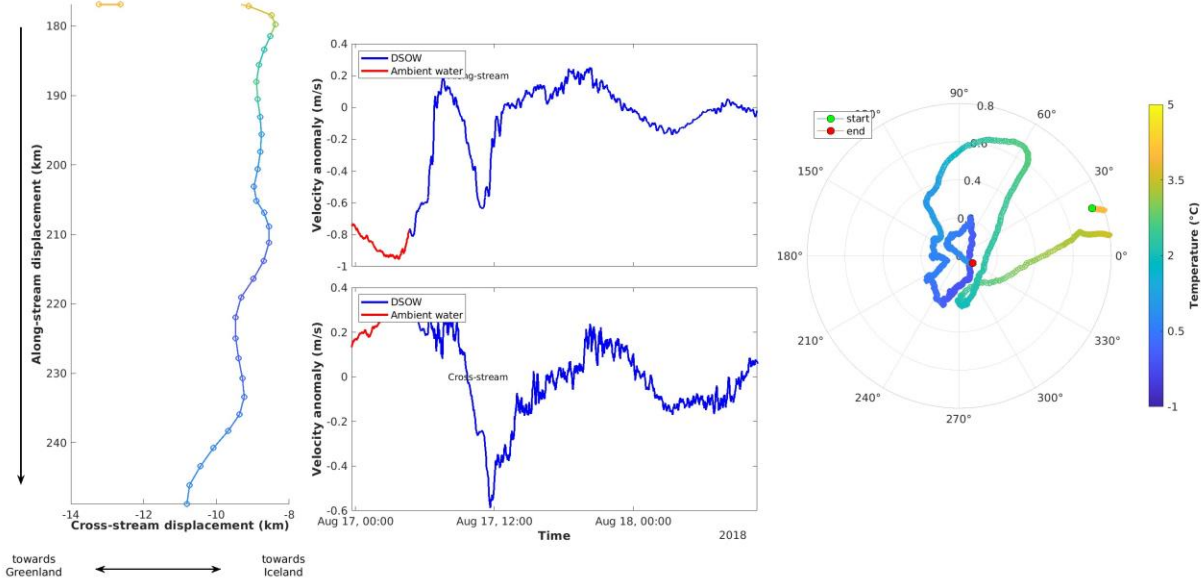


**Figure 35.** Figure 11.2 for the bottom velocimeter.

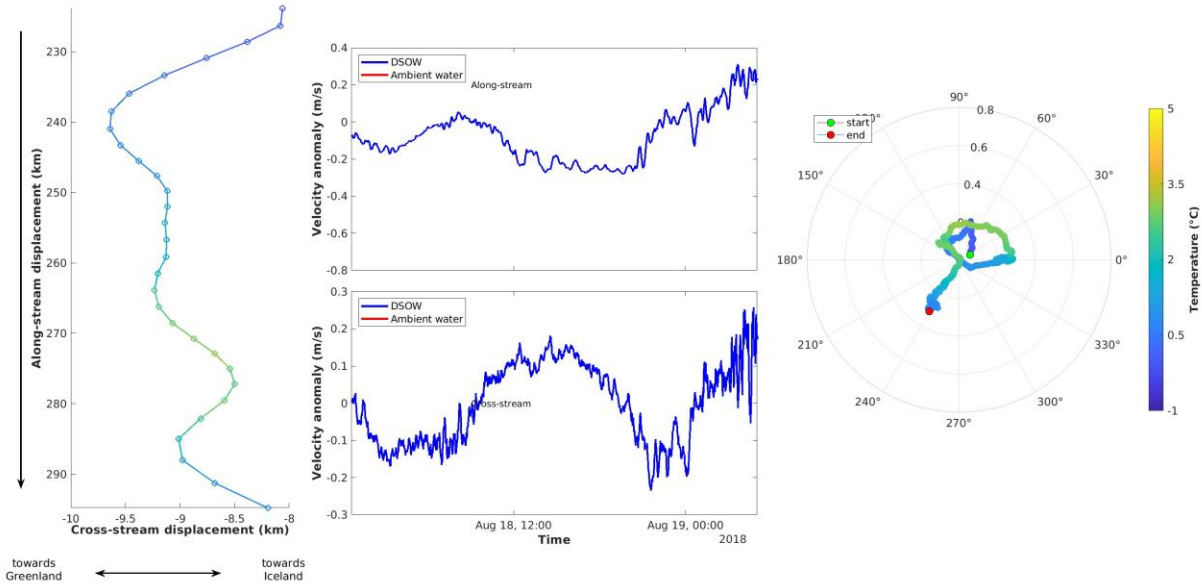


**Figure 36.** Figure 12.2 for the bottom velocimeter.

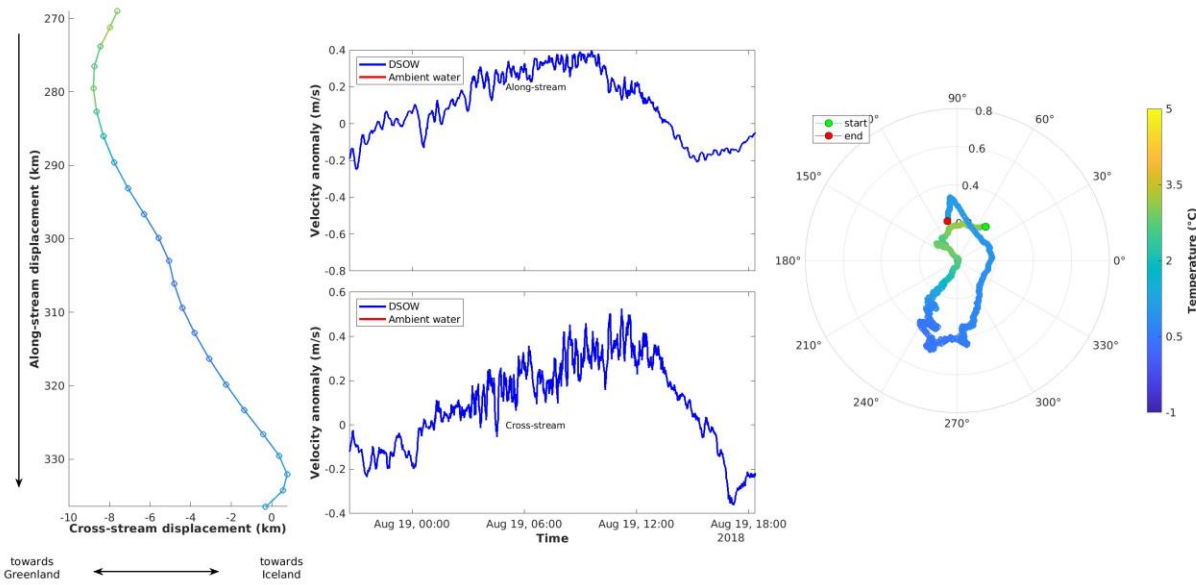


**Figure 37.** Figure 11.3 for the bottom velocimeter.

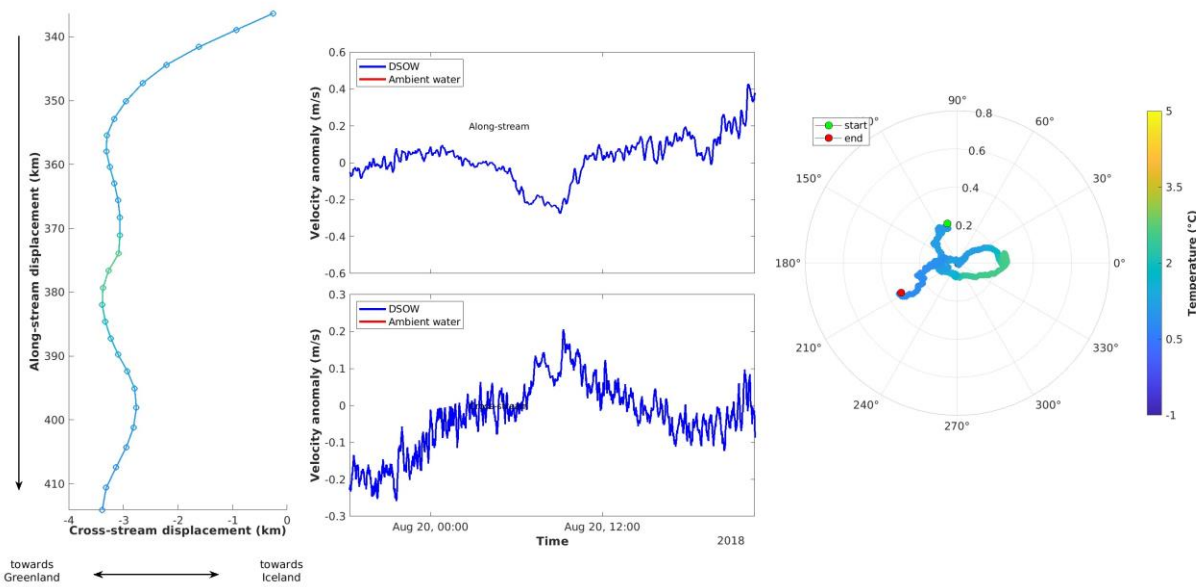


**Figure 38.** Figure 12.3 for the bottom velocimeter.

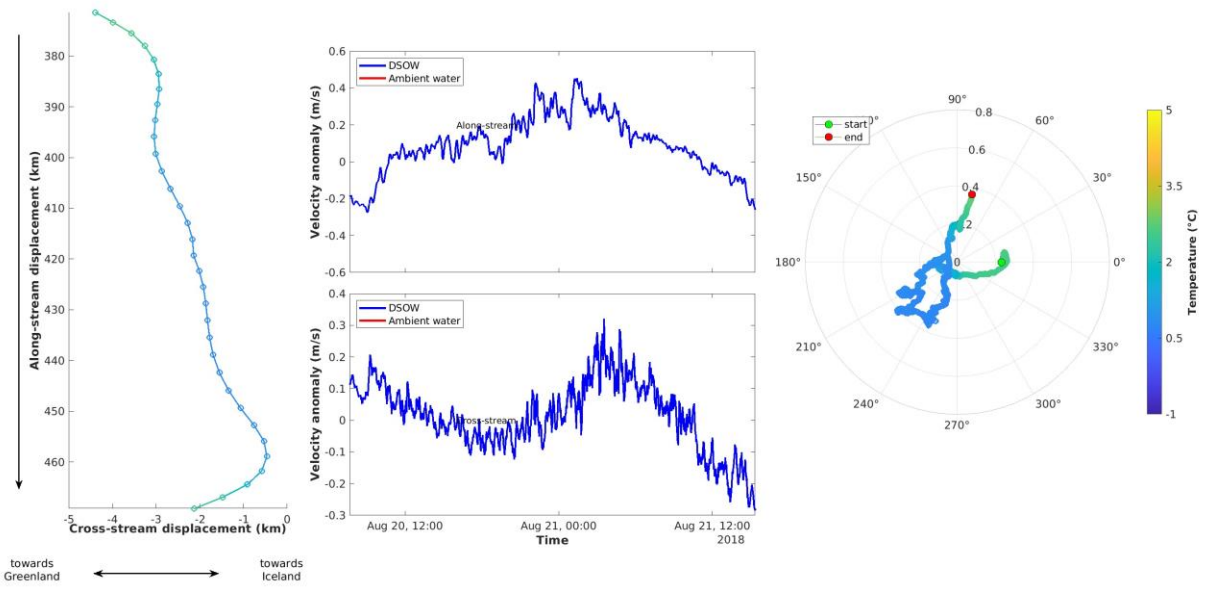


**Figure 39.** Figure 11.4 for the bottom velocimeter.

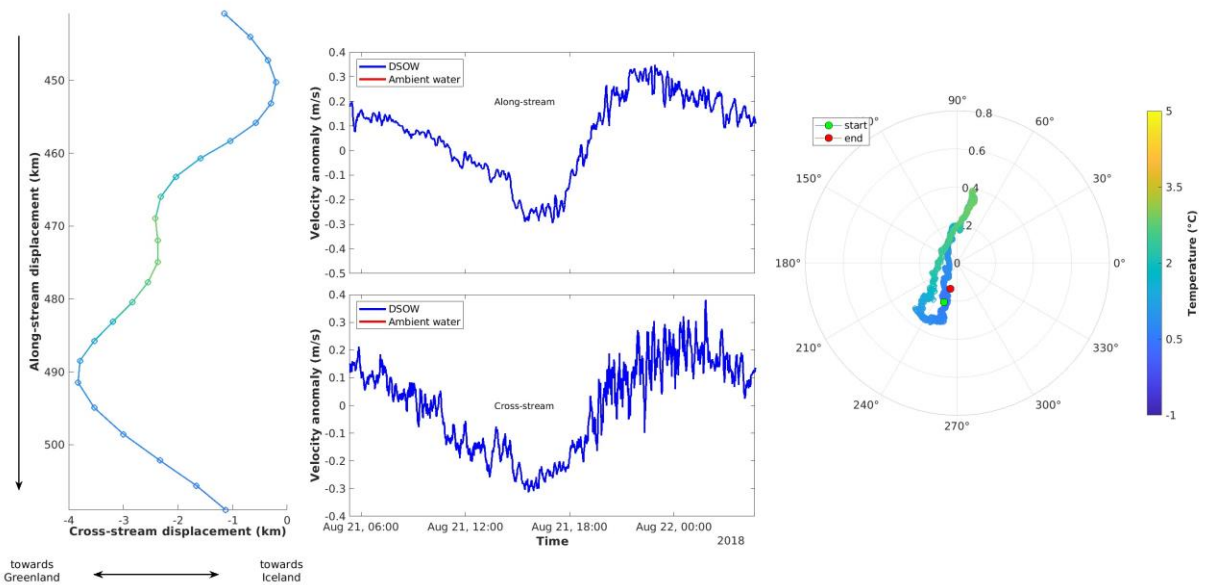


**Figure 40.** Figure 12.4 for the bottom velocimeter.

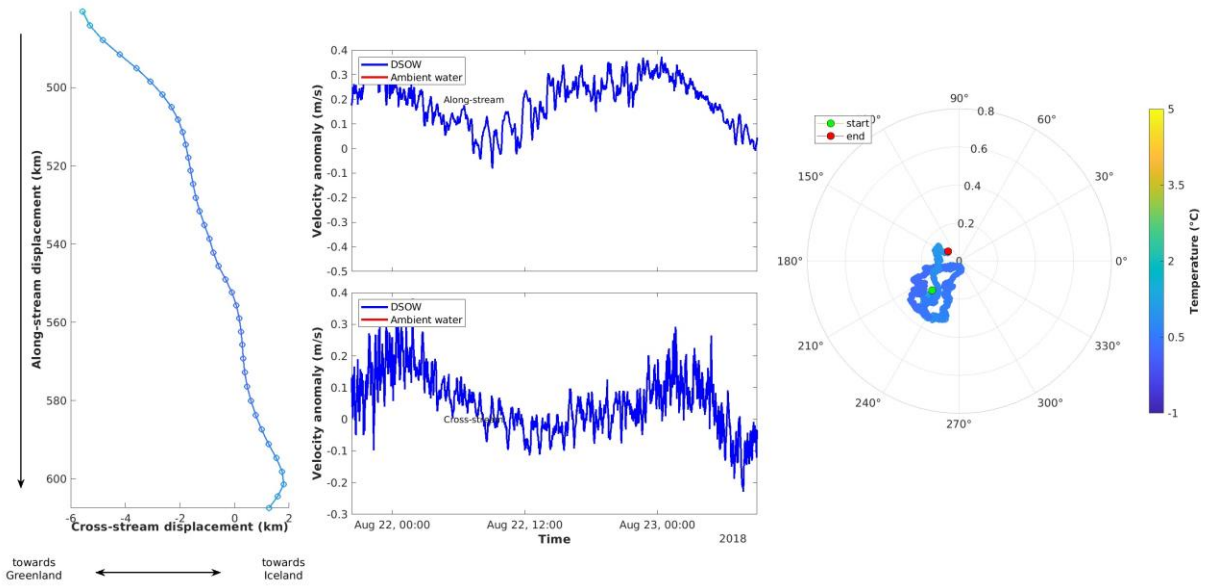


**Figure 41.** Figure 11.5 for the bottom velocimeter.

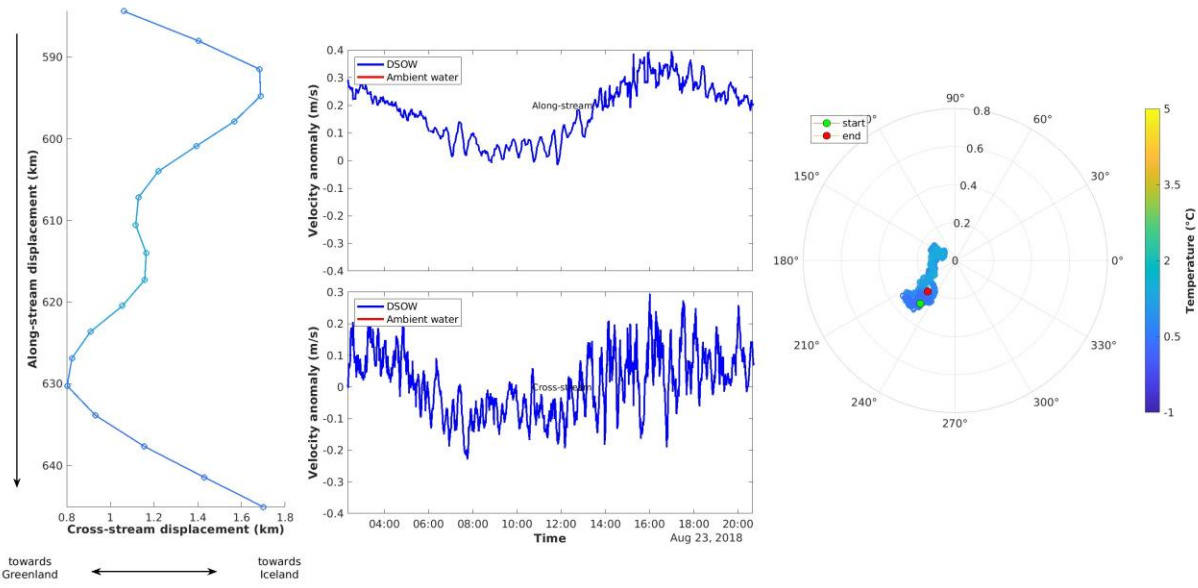


**Figure 42.** Figure 12.5 for the bottom velocimeter.

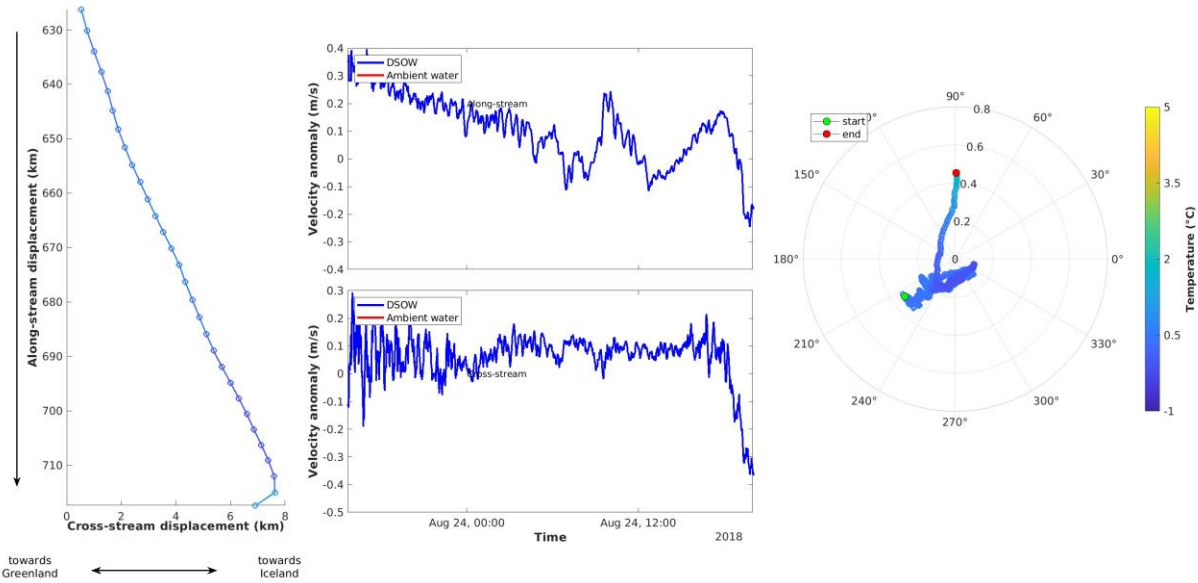


**Figure 43.** Figure 11.6 for the bottom velocimeter.

Hiermit versichere ich an Eides statt, dass ich die vorliegende Arbeit im Studiengang MSc Ocean and Climate Physics selbstständig verfasst und keine anderen als die angegebenen Hilfsmittel – insbesondere keine im Quellenverzeichnis nicht benannten Internet-Quellen – benutzt habe. Alle Stellen, die wörtlich oder sinngemäß aus Veröffentlichungen entnommen wurden, sind als solche kenntlich gemacht. Ich versichere weiterhin, dass ich die Arbeit vorher nicht in einem anderen Prüfungsverfahren eingereicht habe.

Sofern im Zuge der Erstellung der vorliegenden Abschlussarbeit auf generativer künstlicher Intelligenz (gKI) basierte elektronische Hilfsmittel verwendet wurden, versichere ich, dass meine eigene Leistung im Vordergrund stand und dass eine vollständige Dokumentation aller verwendeten Hilfsmittel gemäß der Guten Wissenschaftlichen Praxis vorliegt. Ich trage die Verantwortung für eventuell durch die gKI generierte fehlerhafte oder verzerrte Inhalte, fehlerhafte Referenzen, Verstöße gegen das Datenschutz- und Urheberrecht oder Plagiate.

Einer Veröffentlichung der vorliegenden Arbeit in der zuständigen Fachbibliothek des Fachbereichs stimme ich zu.

<b>Location</b>	<b>Date</b>	<b>Signature</b>
Hamburg	31. December 2024	